On the effect of detwinning-induced plasticity in compressive cyclic loading of NiTi shape memory alloys

Parvin Ebrahimi[a,1] Jamal Arghavani[a,*], Reza Naghdabadi[a,b], J. Patrick McGarry[c]

[a]Mechanical engineering department, Sharif University of Technology, Tehran, Iran

[b]Institute for Nano-Science and Technology, Sharif University of Technology, Tehran, Iran

[c]School of Engineering, National University of Ireland Galway, Ireland

Abstract

A new inelastic mechanism, detwinning-induced plasticity (DIP), is proposed to model the response of NiTi SMAs to cyclic loading, based on thermodynamic considerations. DIP is incorporated into a constitutive framework for NiTi SMA. The constitutive framework also includes well-established inelastic mechanisms of phase transformation, transformation-induced plasticity, residual martensite, and detwinning. The model is constructed at the single crystal scale using the framework of thermodynamics and a crystal plasticity formulation. An explicit scale-transition rule is adopted for the simulation of polycrystalline materials, allowing direct comparison of the model predictions with published experimental test data. Thermodynamic considerations result in a strong contribution of DIP for cyclic loading regimes where compressive stress occurs during part of the loading cycle. However, the contribution of DIP is negligible for cyclic loading regimes that result exclusively in tensile stress. This predicted dependence of DIP on compression, but not on tension, is strongly supported by experimental cyclic loading results. Inclusion of DIP results in improved prediction of experimentally observed NiTi SMAs behavior, including strain-controlled cyclic compression-unloading and cyclic tension-unloading tests and stress-controlled cyclic tension-compression and tension-unloading tests. During the first loading cycle the contribution of DIP is not significant in any loading regimes. However, in cases where compressive stress occurs during part of the loading cycle, DIP contributes strongly to the material response from the second cycle onwards. In strain-controlled cyclic compression-unloading tests DIP leads to a less negative peak stress and a more negative residual strain following several loading cycles. In stress-controlled tension-compression cyclic loading DIP leads to a reduction of peak and residual strains.

Keywords: NiTi; Cyclic loading; Detwining-induced plasticity; Constitutive modeling; Crystal plasticity

[1] Currently visiting researcher at National University of Ireland, Galway

*Corresponding author: arghavani@sharif.edu

1. Introduction

Shape memory alloys (SMAs) have unique characteristics such as super-elasticity, shape memory effect, and high damping capacity. Such characteristics make them suitable for diverse applications such as biomedical devices, sensors, and actuators in micro-electro-mechanical systems, aerospace, automotive, and robotics structures (Hartl and Lagoudas, 2007; Otsuka and Ren, 1999). Of the different categories of SMAs, NiTi alloys are the most common due to high energy density, corrosion resistance, and biocompatibility (Hartl and Lagoudas, 2007).

The behavior of NiTi SMA is completely dependent on the testing temperature. In the absence of stress, a reduction in temperature will transform austenite to twinned martensite. At temperatures lower than the martensite finish-temperature the alloy consists of the original twinned martensite phase. Application of sufficient stress to twinned martensite will cause the production of inelastic strain which is not recovered by removal of the stress, but is recovered during subsequent heating process. This behavior is known as shape memory effect in NiTi SMAs. At temperatures higher than the austenite finish-temperature, the alloy consists of austenite phase. The stress-induced phase transformation leads to strain generation during loading, and subsequent strain recovery upon unloading. This behavior is known as the super-elasticity effect in NiTi shape memory alloys.

Most applications of super-elastic NiTi entail cyclic loading, which can induce changes in the microstructure and can cause macroscopically observable changes in the material behavior. Many experiments have investigated the effects of cyclic loading on the behavior of NiTi SMAs. The start-stress of forward transformation, and the dissipation energy, are found to decrease with increasing loading cycles, whereas transformation hardening is found to increase (Eggeler et al., 2004; Kang et al., 2009). The peak and residual strains are found to increase up to a saturated level with increasing loading cycles (Kang et al., 2009; Nemat-Nasser and Guo, 2006; Saleeb et al., 2013; Song et al., 2014).

Microstructural changes of NiTi SMA under cyclic loadings have also been extensively investigated (Ammar et al., 2017; Brinson et al., 2004; Chen et al., 2019; Delville et al., 2011; Liu and Xie, 2007; Liu et al., 1998; Xie et al., 1998). Under cyclic loading, when the strain is positive similar mechanisms are involved in the generation of compressive and tensile stresses, as discussed by Liu and Xie (2007). However, when the strain is negative, different mechanisms are involved in the generation of tensile and compressive stresses (Liu, 2002; Liu and Xie, 2007; Liu et al., 1998). Detwinning is defined as the movement of interfaces/twin boundaries between lattice

correspondent variants (Thamburaja, 2005; Thamburaja et al., 2005). Each martensite habit plane variant (or simply variant) is composed of two lattice correspondent variants. For simplicity, lattice correspondent variants are referred to as sub-variants (Yu et al., 2014). The microscopic observations show a high density of dislocations at the interfaces of sub-variants during compressive loading while no significant plastic deformation has been detected in these areas under tension (Liu and Xie, 2007; Liu et al., 1998; Xie et al., 1998). Since one of the main inelastic deformation mechanisms for super-elastic NiTi is detwinning, and this kind of plasticity occurs at the interface of sub-variants, this phenomenon is referred to as detwinning-induced plasticity (DIP) hereafter. In an effort to develop an improved model for NiTi SMAs, a constitutive law for DIP is proposed and implemented in the current study. Phenomena such as detwinning-induced plasticity and transformation-induced plasticity generate irrecoverable strains which will accumulate during cyclic loading. In contrast, austenite to martensite transformation results in strains that are recoverable, either by unloading (super-elasticity effect) or by temperature increase (shape memory effect) (Lagoudas, 2008).

Based on experimental observations, many constitutive models have been derived to describe the behavior of SMAs. These models can be classified into two main groups: macroscopic models and micromechanical models. The macroscopic models are suitable for finite element implementation and are readily applicable to structural analysis. However, the underlying microscale physical mechanisms of SMA behavior are not reflected in macroscale phenomenological constitutive models. Representative macroscopic SMA models include Auricchio et al. (2007), Lagoudas et al. (2012), Panico and Brinson (2007), Zaki and Moumni (2007), Arghavani et al. (2010), and Xu et al. (2019).

Many micromechanical constitutive models have been constructed to incorporate the microscopic physical nature of deformation of NiTi SMAs. Micromechanical models based on crystal plasticity formulation are popular since martensite variants with different morphological features and their evolution laws during deformation can be implemented in such a framework. These models are constructed at the scale of a single crystal and then transformed to a polycrystalline scale using either the finite element method, or scale-transition rules. Typical constitutive models include Thamburaja and Anand (2001), Anand and Gurtin (2003), Thamburaja (2005), Thamburaja et al. (2005), Wang et al. (2008), Yu et al. (2012; 2013; 2014, 2015), and Dhala et al. (2019). Thamburaja and Anand have developed a constitutive model for austenite to martensite phase transformation in textured super-elastic NiTi SMAs (Thamburaja and Anand, 2001). The thermo-

mechanically coupled behavior of super-elastic SMAs considering phase transformation have been investigated by Anand and Gurtin (2003). In order to consider the effects of detwinning and reorientation, a constitutive model was proposed by Thamburaja (2005). This model was modified to include austenite to martensite phase transformation (Thamburaja et al., 2005). The interactions between phase transformation and plasticity in austenite and martensite phases have also been investigated (Dhala et al., 2019; Manchiraju and Anderson, 2010; Wang et al., 2008; Yu et al., 2014). In order to simulate the behavior of SMAs under cyclic loadings, Yu et al. (2013, 2015) proposed a constitutive law that incorporates a number of inelastic mechanisms, including: austenite to martensite phase transformation, reorientation, transformation-induced plasticity, reorientation-induced plasticity, and accumulation of residual martensite. While previous studies have considered effects such as phase transformation, transformation-induced plasticity, detwinning, and accumulation of residual martensite (Dhala et al., 2019; Thamburaja and Anand, 2001; Thamburaja et al., 2005; Wang et al., 2008; Xiao et al., 2018; Yu et al., 2014; Yu et al., 2013; Yu et al., 2015), the effect of DIP has not been previously considered.

The goal of the current study is to incorporate the effect of detwinning-induced plasticity into a constitutive model for NiTi SMAs. To this end, a constitutive model is proposed based on crystal plasticity and, for the first time, the inelastic mechanism of detwinning-induced plasticity is incorporated. The model is developed at the single crystal scale and also includes phase transformation, transformation-induced plasticity, detwinning, and accumulation of residual martensite. Adopting a new Helmholtz free energy and using the framework of thermodynamics, the driving forces for inelastic mechanisms are derived. An explicit scale-transition rule (Yu et al., 2014; Yu et al., 2013; Yu et al., 2012, 2015) is used to obtain the polycrystalline response from that of single crystal. The improved predictive capability of the proposed DIP constitutive law is demonstrated by comparing model results with published cyclic stress-controlled and strain-controlled experimental data.

2. Micromechanical constitutive model

2.1. Single crystal constitutive model in the framework of thermodynamics

Considering small deformation, the total strain tensor in a representative volume element (RVE) of a single crystal is decomposed into five components: elastic strain tensor $\boldsymbol{\varepsilon}^{e}$, transformation strain tensor $\boldsymbol{\varepsilon}^{tr}$, transformation-induced plastic strain tensor $\boldsymbol{\varepsilon}^{TRIP}$, detwinning strain tensor $\boldsymbol{\varepsilon}^{det}$, and detwinning-induced plastic strain tensor $\boldsymbol{\varepsilon}^{DIP}$. The total stain tensor, $\boldsymbol{\varepsilon}$, and the inelastic strain tensor, $\boldsymbol{\varepsilon}^{in}$, are given as:

$$\boldsymbol{\varepsilon} = \boldsymbol{\varepsilon}^{e} + \boldsymbol{\varepsilon}^{in} \tag{1.a}$$

$$\boldsymbol{\varepsilon}^{in} = \boldsymbol{\varepsilon}^{tr} + \boldsymbol{\varepsilon}^{TRIP} + \boldsymbol{\varepsilon}^{det} + \boldsymbol{\varepsilon}^{DIP} \tag{1.b}$$

24 variants are present in the transformed martensite of NiTi shape memory alloy. The transformation strain of each martensite variant can be calculated from the normal and transformation direction of its habit plane. Therefore, the total transformation strain can be calculated considering the contribution of each variant (Patoor et al., 2006):

$$\boldsymbol{\varepsilon}^{tr} = \sum_{\alpha=1}^{24} \xi^{\alpha} g^{tr} \mathbf{P}^{\alpha} \tag{2.a}$$

$$\mathbf{P}^{\alpha} = \frac{1}{2}\left(\mathbf{m}^{\alpha} \otimes \mathbf{n}^{\alpha} + \mathbf{n}^{\alpha} \otimes \mathbf{m}^{\alpha}\right) \tag{2.b}$$

where $\boldsymbol{\varepsilon}^{tr}$ is the total transformation strain caused by austenite to martensite transformation, ξ^{α} is the volume fraction of the α-th martensite variant, and g^{tr} is the magnitude of shearing deformation caused by martensite transformation. $\mathbf{P}^{\alpha}$ is the orientation tensor of the α-th martensite variant which is related to transformation direction $\mathbf{m}^{\alpha}$, and habit plane normal $\mathbf{n}^{\alpha}$, of the α-th martensite variant. The magnitudes of habit plane normal $\mathbf{n}^{\alpha}$ and transformation direction $\mathbf{m}^{\alpha}$ of 24 variants are listed in the Appendix.

As experimentally observed (Brinson et al., 2004; Kang et al., 2009), during cyclic loading some part of martensite will not transform back to austenite even when the load is completely removed. This part of martensite, which is pinned by the increase of defects, is called residual martensite. Therefore, the volume fraction of each martensite variant can be divided into two parts, i.e. the reversible martensite volume fraction ξ_{rev}^{α} and the irreversible (residual) martensite volume fraction ξ_{ire}^{α}. The total volume fraction of martensite is obtained by summing the reversible and irreversible parts of each variant.

$$\xi^{\alpha} = \xi_{rev}^{\alpha} + \xi_{ire}^{\alpha} \tag{3.a}$$

$$\xi = \sum_{\alpha=1}^{24} \xi^{\alpha}, \qquad \xi_{rev} = \sum_{\alpha=1}^{24} \xi_{rev}^{\alpha}, \qquad \xi_{ire} = \sum_{\alpha=1}^{24} \xi_{ire}^{\alpha} \tag{3.b}$$

Considering reversible and residual parts for each martensite variant, the transformation strain can be re-written as:

$$\boldsymbol{\varepsilon}^{tr} = \boldsymbol{\varepsilon}_{rev}^{tr} + \boldsymbol{\varepsilon}_{ire}^{tr} = \sum_{\alpha=1}^{24} \xi_{rev}^{\alpha} g^{tr} \mathbf{P}^{\alpha} + \sum_{\alpha=1}^{24} \xi_{ire}^{\alpha} g^{tr} \mathbf{P}^{\alpha} \tag{4}$$

Due to the misfit at some interfaces, a local stress field is induced at these areas. Plastic deformation will occur to relax this local stress. As discussed by Kang et al. (2009), transformation-induced plasticity (TRIP) is caused by irreversible friction slip at austenite-martensite interfaces. Assuming the same orientation for transformation and transformation-induced plasticity, the strain caused by TRIP can be divided into 24 components (Yu et al., 2013):

$$\boldsymbol{\varepsilon}^{TRIP} = \sum_{\alpha=1}^{24} \gamma_{TRIP}^{\alpha} \mathbf{P}^{\alpha} \tag{5}$$

where $\boldsymbol{\varepsilon}^{TRIP}$ is the transformation-induced plastic strain tensor and γ_{TRIP}^{α} is the amount of slipping caused by transformation-induced plasticity at the interface of austenite and the α-th martensite variant.

As discussed by Thamburaja (2005) and Thamburaja et al. (2005), austenite to martensite phase transformation will occur in the absence of stress if temperature is decreased to a value lower than the martensite finish-temperature. This transformation will cause martensitic plates or habit plane variants (HPVs) to form. The martensite within the HPVs comprises of two lattice correspondent variants (LCVs), which are called sub-variants in this paper. The HPVs and LCVs are separated by interfaces. The movement of interfaces/twin boundaries between LCVs, which is motivated by the application of stress, is referred to as detwinning. As detwinning occurs inside each variant, this contribution is divided into 24 components:

$$\boldsymbol{\varepsilon}^{det} = \sum_{\alpha=1}^{24} \xi^{\alpha} \left(\lambda^{\alpha} - \lambda_0^{\alpha} \right) \mathbf{P}_{det}^{\alpha} \tag{6.a}$$

$$\mathbf{P}_{det}^{\alpha} = \frac{1}{2} \left(\mathbf{a}^{\alpha} \otimes \mathbf{w}^{\alpha} + \mathbf{w}^{\alpha} \otimes \mathbf{a}^{\alpha} \right) \tag{6.b}$$

where the initial volume fractions of two sub-variants in the α-th martensite variant are λ_0^{α} and 1-λ_0^{α}. λ^{α} and 1-λ^{α} are current volume fractions of two sub-variants, and $\left(\lambda^{\alpha} - \lambda_0^{\alpha} \right)$ represents

the amount transformed from one sub-variant to the other. $\mathbf{P}_{det}^{\alpha}$ is the orientation tensor for the α-th detwinning system which is related to shear direction for detwinning $\mathbf{w}^{\alpha}$, and unit vector normal to detwinning plane $\mathbf{a}^{\alpha}$, of the α-th martensite variant. The crystallographic data for different detwinning systems are listed in the Appendix.

Experimental observations of SMAs undergoing cyclic loading show that some part of the developed strain is not recovered after unloading and accumulates with every transformation cycle. Such plasticity can be activated even when the applied stress is much lower than the yielding stress of austenite and martensite phases (Lagoudas, 2008). DIP is related to the part of the irrecoverable strain induced to relax the local stress field at the interfaces of sub-variants. Using the same orientation tensor for detwinning and DIP, a DIP strain tensor is proposed as follows:

$$\boldsymbol{\varepsilon}^{DIP} = \sum_{\alpha=1}^{24} \gamma_{DIP}^{\alpha} \mathbf{P}_{det}^{\alpha} \tag{7}$$

where γ_{DIP}^{α} is the amount of shearing deformation caused by detwinning-induced plasticity in the α-th martensite variant.

The Helmholtz free energy of RVE is considered to be composed of five parts:

$$\psi = \psi^{e} + \psi^{ch} + \psi^{\text{int}} + \psi_{rev}^{tr} + \psi^{det} \tag{8}$$

where ψ^{e} represents the elastic energy of RVE and is dependent on the elastic strain tensor, such that:

$$\psi^{e}\left(\boldsymbol{\varepsilon}^{e}\right) = \frac{1}{2}\boldsymbol{\varepsilon}^{e} : \mathbf{C} : \boldsymbol{\varepsilon}^{e} \tag{9.a}$$

where $\mathbf{C}$ is the fourth-order elasticity tensor, which is considered to be isotropic for simplicity.

ψ^{ch} is the chemical energy of RVE which reflects the effect of ambient temperature on the transformation:

$$\psi^{ch}\left(T,\xi\right) = c\left[\left(T-T_0\right) - T\ln\left(\frac{T}{T_0}\right)\right] + \beta\left(T-T_0\right)\xi \tag{10}$$

where T_0 is reference temperature, c is specific heat capacity and β is a constant.

ψ^{int} is the part of free energy which reflects the effect of internal stress and is adopted similar to the work done by Yu et al. (2013). The role of ψ^{int} is given as

$$\dot{\psi}^{\text{int}} = -\mathbf{B} : \dot{\boldsymbol{\varepsilon}}^{in} \tag{11}$$

where $\mathbf{B}$ is the internal stress which is introduced to describe the decrease in the start-stress of martensite transformation during cyclic loading. The internal stress facilitates the start of transformation and therefore decreases the start-stress of phase transformation. As the internal stress is caused by martensite variants, it can be divided into 24 components.

$$\mathbf{B} = \sum_{\alpha=1}^{24} \mathbf{B}^{\alpha} \tag{12}$$

where $\mathbf{B}^{\alpha}$ is the internal stress caused by the α-th martensite variant. The orientation of $\mathbf{B}^{\alpha}$ is assumed to be the same as the corresponding martensite variant transformation direction and is expressed as:

$$\mathbf{B}^{\alpha} = \left\| \mathbf{B}^{\alpha} \right\| \mathbf{P}^{\alpha} \tag{13}$$

where $\left\| \mathbf{B}^{\alpha} \right\|$ is the norm of $\mathbf{B}^{\alpha}$. For simplicity, it is assumed that the internal stress is a function of accumulated martensite volume fraction ξ_c^{α} (Yu et al., 2013):

$$\left\| \mathbf{B}^{\alpha} \right\| = \mathrm{B}_{\text{sat}} \left(1 - \exp\left(-\xi_c^{\alpha} / b_1 \right) \right) \tag{14.a}$$

$$\dot{\xi}_c^{\alpha} = \left| \dot{\xi}_{rev}^{\alpha} \right| \tag{14.b}$$

b_1 is the parameter which controls the saturation rate of $\left\| \mathbf{B}^{\alpha} \right\|$.

ψ_{rev}^{tr} and ψ^{det} are the energetic contributions due to hardening and softening effects during cyclic loading for transformation and detwinning, respectively. The rates of ψ_{rev}^{tr} and ψ^{det} are given as:

$$\dot{\psi}_{rev}^{tr} = \sum_{\alpha=1}^{24} \mathrm{X}^{\alpha} \dot{\xi}_{rev}^{\alpha} \tag{15.a}$$

$$\dot{\psi}^{det} = \sum_{\alpha=1}^{24} \mathrm{X}_{\text{det}}^{\alpha} \left| \dot{\lambda}^{\alpha} \right| \tag{15.b}$$

where X^{α} and $\mathrm{X}_{\text{det}}^{\alpha}$ are the transformation and detwinning resistances of the α-th martensite variant, respectively.

As transformation hardening occurs during cyclic deformation, X^{α} is considered as a function of the reversible martensite volume fraction.

$$\mathrm{X}^{\alpha} = H^{\alpha}\xi_{rev}^{\alpha} \tag{16.a}$$

$$H^{\alpha} = H_0 + \left(H_{sat} - H_0\right)\left(1 - \exp\left(-\frac{\xi_c^{\alpha}}{b_2}\right)\right) \tag{16.b}$$

where H^{α} is a hardening modulus and a function of accumulated martensite volume fraction ξ_c^{α}. H_0 and H_{sat} are initial and saturation values of H^{α}, respectively. The parameter b_2 controls the evolution rate of H^{α} during cyclic loading.

The hardening equation for detwinning resistance is based on (Yu et al., 2014) and is expressed as:

$$\dot{\mathrm{X}}_{\mathrm{det}}^{\alpha} = h_{\mathrm{det}}\left|\dot{\lambda}^{\alpha}\right| \tag{17}$$

where h_{det} is the hardening modulus for detwinning.

Using the 2nd law of thermodynamics and the Helmholtz free energy, the Clausius dissipation inequality can be written as:

$$\Gamma = \boldsymbol{\sigma} : \dot{\boldsymbol{\varepsilon}} - \dot{\psi} - \eta\dot{T} - \frac{\mathbf{q}.\nabla T}{T} \geq 0 \tag{18}$$

By the assumption of quasi-static loading, the temperature in a single crystal can be considered to be homogeneous. Therefore, neglecting the effect of transformation latent heat and the heat generated from internal dissipation, the Clausius dissipation inequality is expressed as:

$$\Gamma = \boldsymbol{\sigma} : \dot{\boldsymbol{\varepsilon}} - \dot{\psi} - \eta\dot{T} \geq 0 \tag{19}$$

Using equations (1), (9-11), and (15) yields:

$$\begin{aligned}
&\Gamma = \boldsymbol{\sigma} : \dot{\boldsymbol{\varepsilon}}^{e} + \boldsymbol{\sigma} : \dot{\boldsymbol{\varepsilon}}^{tr} + \boldsymbol{\sigma} : \dot{\boldsymbol{\varepsilon}}^{TRIP} + \boldsymbol{\sigma} : \dot{\boldsymbol{\varepsilon}}^{det} + \boldsymbol{\sigma} : \dot{\boldsymbol{\varepsilon}}^{DIP} \\
&- \frac{\partial \psi^{e}\left(\boldsymbol{\varepsilon}^{e}\right)}{\partial \boldsymbol{\varepsilon}^{e}} : \dot{\boldsymbol{\varepsilon}}^{e} - \frac{\partial \psi^{ch}\left(T,\xi\right)}{\partial T}\dot{T} - \frac{\partial \psi^{ch}\left(T,\xi\right)}{\partial \xi}\dot{\xi} \\
&+ \mathbf{B} : \left(\dot{\boldsymbol{\varepsilon}}^{tr} + \dot{\boldsymbol{\varepsilon}}^{TRIP} + \dot{\boldsymbol{\varepsilon}}^{det} + \dot{\boldsymbol{\varepsilon}}^{DIP}\right) - \sum_{\alpha=1}^{24} \mathrm{X}^{\alpha}\dot{\xi}_{rev}^{\alpha} - \sum_{\alpha=1}^{24} \xi^{\alpha}\mathrm{X}_{\mathrm{det}}^{\alpha}\left|\dot{\lambda}^{\alpha}\right| - \eta\dot{T} \geq 0
\end{aligned} \tag{20}$$

Considering the special case when $\dot{\xi}_{rev}^{\alpha}=\dot{\xi}_{ire}^{\alpha}=\dot{\gamma}_{TRIP}^{\alpha}=\dot{\lambda}^{\alpha}=\dot{\gamma}_{DIP}^{\alpha}=0$ and using the methodology of Coleman and Noll (1974), since $\dot{\boldsymbol{\varepsilon}}^{e}$ and $\dot{T}$ can assume either positive or negative values, Eq. (20) can only be satisfied through the requirement that:

$$\boldsymbol{\sigma}=\frac{\partial\psi^{e}\left(\boldsymbol{\varepsilon}^{e}\right)}{\partial\boldsymbol{\varepsilon}^{e}}=\mathbf{C}:\boldsymbol{\varepsilon}^{e} \tag{21.a}$$

$$\eta=-\frac{\partial\psi^{ch}\left(T,\xi\right)}{\partial T}=c\ln\left(\frac{T}{T_{0}}\right)-\beta\xi \tag{21.b}$$

The dissipation inequality can be re-written as:

$$\begin{aligned}\Gamma=&\left(\boldsymbol{\sigma}+\mathbf{B}\right):\left(\sum_{\alpha=1}^{24}\dot{\xi}_{rev}^{\alpha}g^{tr}\mathbf{P}^{\alpha}+\sum_{\alpha=1}^{24}\dot{\xi}_{ire}^{\alpha}g^{tr}\mathbf{P}^{\alpha}+\sum_{\alpha=1}^{24}\dot{\gamma}_{TRIP}^{\alpha}\mathbf{P}^{\alpha}\right)\\&+\left(\boldsymbol{\sigma}+\mathbf{B}\right):\left(\sum_{\alpha=1}^{24}\dot{\xi}^{\alpha}\left(\lambda^{\alpha}-\lambda_{0}^{\alpha}\right)\mathbf{P}_{det}^{\alpha}+\sum_{\alpha=1}^{24}\xi^{\alpha}\dot{\lambda}^{\alpha}\mathbf{P}_{det}^{\alpha}+\sum_{\alpha=1}^{24}\dot{\gamma}_{DIP}^{\alpha}\mathbf{P}_{det}^{\alpha}\right)\\&-\frac{\partial\psi^{ch}\left(T,\xi\right)}{\partial\xi}\dot{\xi}-\sum_{\alpha=1}^{24}\mathrm{X}^{\alpha}\dot{\xi}_{rev}^{\alpha}-\sum_{\alpha=1}^{24}\mathrm{X}_{\mathrm{det}}^{\alpha}\left|\dot{\lambda}^{\alpha}\right|\geq0\end{aligned} \tag{22}$$

Since reversible and residual martensite transformation, TRIP, detwinning, and DIP are all dissipative phenomena, the strong form requires that each part is non-negative such that:

$$\Gamma_{tr,rev}=\sum_{\alpha=1}^{24}\left[\left(\boldsymbol{\sigma}+\mathbf{B}\right):\left(g^{tr}\mathbf{P}^{\alpha}+\left(\lambda^{\alpha}-\lambda_{0}^{\alpha}\right)\mathbf{P}_{det}^{\alpha}\right)-\frac{\partial\psi^{ch}\left(T,\xi\right)}{\partial\xi}-\mathrm{X}^{\alpha}\right]\dot{\xi}_{rev}^{\alpha}\geq0 \tag{23.a}$$

$$\Gamma_{tr,ire}=\sum_{\alpha=1}^{24}\left[\left(\boldsymbol{\sigma}+\mathbf{B}\right):\left(g^{tr}\mathbf{P}^{\alpha}+\left(\lambda^{\alpha}-\lambda_{0}^{\alpha}\right)\mathbf{P}_{det}^{\alpha}\right)-\frac{\partial\psi^{ch}\left(T,\xi\right)}{\partial\xi}\right]\dot{\xi}_{ire}^{\alpha}\geq0 \tag{23.b}$$

$$\Gamma_{TRIP}=\sum_{\alpha=1}^{24}\left(\boldsymbol{\sigma}+\mathbf{B}\right):\mathbf{P}^{\alpha}\dot{\gamma}_{TRIP}^{\alpha}\geq0 \tag{23.c}$$

$$\Gamma_{det}=\sum_{\alpha=1}^{24}\left[\left(\boldsymbol{\sigma}+\mathbf{B}\right):\xi^{\alpha}\mathbf{P}_{det}^{\alpha}\dot{\lambda}^{\alpha}-\mathrm{X}_{\mathrm{det}}^{\alpha}\left|\dot{\lambda}^{\alpha}\right|\right]\geq0 \tag{23.d}$$

$$\Gamma_{DIP}=\sum_{\alpha=1}^{24}\left(\boldsymbol{\sigma}+\mathbf{B}\right):\mathbf{P}_{det}^{\alpha}\dot{\gamma}_{DIP}^{\alpha}\geq0 \tag{23.e}$$

It is assumed that the dissipation inequality is non-negative for all variants. Therefore, each dissipation part in Eq. (23) can be divided into 24 components, i.e.,

$$\Gamma_{tr,rev}^{\alpha}=\left[\begin{array}{c}\left(\boldsymbol{\sigma}+\mathbf{B}\right):\left(g^{tr}\mathbf{P}^{\alpha}+\left(\lambda^{\alpha}-\lambda_{0}^{\alpha}\right)\mathbf{P}_{det}^{\alpha}\right)\\ -\dfrac{\partial\psi^{ch}\left(T,\xi\right)}{\partial\xi}-\mathrm{X}^{\alpha}\end{array}\right]\dot{\xi}_{rev}^{\alpha}\geq 0 \qquad \alpha=1,2,...,24 \tag{24.a}$$

$$\Gamma_{tr,ire}^{\alpha}=\left[\left(\boldsymbol{\sigma}+\mathbf{B}\right):\left(g^{tr}\mathbf{P}^{\alpha}+\left(\lambda^{\alpha}-\lambda_{0}^{\alpha}\right)\mathbf{P}_{det}^{\alpha}\right)-\frac{\partial\psi^{ch}\left(T,\xi\right)}{\partial\xi}\right]\dot{\xi}_{ire}^{\alpha}\geq 0 \qquad \alpha=1,2,...,24 \tag{24.b}$$

$$\Gamma_{TRIP}^{\alpha}=\left(\boldsymbol{\sigma}+\mathbf{B}\right):\mathbf{P}^{\alpha}\dot{\gamma}_{TRIP}^{\alpha}\geq 0 \qquad \alpha=1,2,...,24 \tag{24.c}$$

$$\Gamma_{det}^{\alpha}=\left(\boldsymbol{\sigma}+\mathbf{B}\right):\xi^{\alpha}\mathbf{P}_{det}^{\alpha}\dot{\lambda}^{\alpha}-\mathrm{X}_{\mathrm{det}}^{\alpha}\left|\dot{\lambda}^{\alpha}\right|\geq 0 \qquad \alpha=1,2,...,24 \tag{24.d}$$

$$\Gamma_{DIP}^{\alpha}=\left(\boldsymbol{\sigma}+\mathbf{B}\right):\mathbf{P}_{det}^{\alpha}\dot{\gamma}_{DIP}^{\alpha}\geq 0 \qquad \alpha=1,2,...,24 \tag{24.e}$$

In order to satisfy the constraint of thermodynamics, it is assumed that:

$$\mathrm{sign}(\dot{\lambda}^{\alpha})=\mathrm{sign}\left(\left(\boldsymbol{\sigma}+\mathbf{B}\right):\mathbf{P}_{det}^{\alpha}\right) \tag{25}$$

Thus, the thermodynamics driving forces for internal variables can be expressed by:

$$\pi_{tr,rev}^{\alpha}=\left(\boldsymbol{\sigma}+\mathbf{B}\right):\left(g^{tr}\mathbf{P}^{\alpha}+\left(\lambda^{\alpha}-\lambda_{0}^{\alpha}\right)\mathbf{P}_{det}^{\alpha}\right)-\beta\left(T-T_{0}\right)-\mathrm{X}^{\alpha} \quad \alpha=1,2,...,24 \tag{26.a}$$

$$\pi_{tr,ire}^{\alpha}=\left(\boldsymbol{\sigma}+\mathbf{B}\right):\left(g^{tr}\mathbf{P}^{\alpha}+\left(\lambda^{\alpha}-\lambda_{0}^{\alpha}\right)\mathbf{P}_{det}^{\alpha}\right)-\beta\left(T-T_{0}\right) \qquad \alpha=1,2,...,24 \tag{26.b}$$

$$\pi_{TRIP}^{\alpha}=\left(\boldsymbol{\sigma}+\mathbf{B}\right):\mathbf{P}^{\alpha} \qquad \alpha=1,2,...,24 \tag{26.c}$$

$$\pi_{det}^{\alpha}=\left|\left(\boldsymbol{\sigma}+\mathbf{B}\right):\xi^{\alpha}\mathbf{P}_{det}^{\alpha}\right|-\mathrm{X}_{\mathrm{det}}^{\alpha} \qquad \alpha=1,2,...,24 \tag{26.d}$$

$$\pi_{DIP}^{\alpha}=\left(\boldsymbol{\sigma}+\mathbf{B}\right):\mathbf{P}_{det}^{\alpha} \qquad \alpha=1,2,...,24 \tag{26.e}$$

The work conjugate quantities associated with the thermodynamic driving forces are listed below:

$$\pi_{tr,rev}^{\alpha}\leftrightarrow\dot{\xi}_{rev}^{\alpha} \tag{27.a}$$

$$\pi_{tr,ire}^{\alpha}\leftrightarrow\dot{\xi}_{ire}^{\alpha} \tag{27.b}$$

$$\pi_{TRIP}^{\alpha}\leftrightarrow\dot{\gamma}_{TRIP}^{\alpha} \tag{27.c}$$

$$\pi_{det}^{\alpha}\leftrightarrow\left|\dot{\lambda}^{\alpha}\right| \tag{27.d}$$

$$\pi_{DIP}^{\alpha}\leftrightarrow\dot{\gamma}_{DIP}^{\alpha} \tag{27.e}$$

2.2. Evolution equations for internal variables

2.2.1. Evolution equations for reversible phase transformation

Considering the Clausius inequality for reversible martensite volume fraction, the product of $\dot{\xi}^{\alpha}_{rev}$ and $\pi^{\alpha}_{tr,rev}$ should always be non-negative. During forward transformation $\dot{\xi}^{\alpha}_{rev} > 0$, and for Eq. (24.a) to be satisfied, $\pi^{\alpha}_{tr,rev}$ should be positive. If reverse transformation occurs, $\dot{\xi}^{\alpha}_{rev} < 0$ and $\pi^{\alpha}_{tr,rev}$ should be negative to satisfy the 2nd law of thermodynamics. $\dot{\xi}^{\alpha}_{rev} = 0$ during elastic loading and unloading without any martensite transformation, so that Eq. (24.a) is automatically satisfied.

Using the concept of transformation functions (Lagoudas and Entchev, 2004; Patoor et al., 2006), the evolution equations for the reversible part of martensite volume fraction are proposed here in the form:

$$\begin{cases} \dot{\xi}^{\alpha}_{rev} = \left| \dfrac{\pi^{\alpha}_{tr,rev}}{Y} \right|^{n_{tr}} & \text{if } \left(\pi^{\alpha}_{tr,rev} > 0, \quad \xi^{\alpha} < 1, \quad \xi < 1 \right) \quad (28.a) \\ \dot{\xi}^{\alpha}_{rev} = -\left| \dfrac{\pi^{\alpha}_{tr,rev}}{K^{tr}} \right|^{n_{tr}} & \text{if } \left(\pi^{\alpha}_{tr,rev} < 0, \quad \xi^{\alpha} > \xi^{\alpha}_{ire}, \quad \xi > \xi_{ire} \right) \\ \dot{\xi}^{\alpha}_{rev} = 0 & \text{other conditions} \quad (28.b) \end{cases}$$

(28.c)

where K^{tr} is constant, and Y is a positive variable which evolves during cyclic loading. The rate sensitivity of martensite transformation is controlled by n_{tr}; a high value of n_{tr} enforces a rate-independent response.

The parameter Y controls the width of hysteresis loop, and is dependent on martensite volume fraction:

$$Y = Y_0 + Y_d \xi_{rev} \quad (29)$$

where Y_0 is the initial value of Y, and Y_d describes the dependence of Y on the current martensite volume fraction.

Based on (Lagoudas and Entchev, 2004), the balance temperature T_0 can be calculated from:

$$T_0 = M_{0s} + \frac{Y}{\beta} \quad (30)$$

where M_{0s} is the martensite start temperature under the stress-free condition.

2.2.2. Evolution equations for transformation-induced plasticity

Since transformation-induced plasticity is an irreversible dissipation process, $\dot{\gamma}_{TRIP}^{\alpha}$ is always non-negative, i.e., $\dot{\gamma}_{TRIP}^{\alpha} \geq 0$. Considering Eq. (24.c), the constraint for TRIP can be described as:

$$\begin{cases} \dot{\gamma}_{TRIP}^{\alpha} > 0 & \pi_{TRIP}^{\alpha} \geq 0 \quad (31.a) \\ \dot{\gamma}_{TRIP}^{\alpha} = 0 & \text{no constraint} \quad (31.b) \end{cases}$$

Using Eq. (31), an evolution equation for TRIP (Yu et al., 2013) can be expressed as:

$$\dot{\gamma}_{TRIP}^{\alpha} = \left(\left\langle \dot{\xi}_{rev}^{\alpha} \right\rangle + \mu_{TRIP} \left\langle -\dot{\xi}_{rev}^{\alpha} \right\rangle \right) \left\langle \frac{G_{TRIP}^{\alpha}\left(\xi_{rev}^{\alpha}\right) - T_{TRIP}^{\alpha}\left(\gamma_{TRIP}^{\alpha}\right)}{D_{TRIP}} \right\rangle H\left(\pi_{TRIP}^{\alpha}\right) \quad (32.a)$$

$$G_{TRIP}^{\alpha}\left(\xi_{rev}^{\alpha}\right) = \left(\xi_{rev}^{\alpha}\right)^{n} \quad (32.b)$$

$$T_{TRIP}^{\alpha}\left(\gamma_{TRIP}^{\alpha}\right) = d_{TRIP}\gamma_{TRIP}^{\alpha} \quad (32.c)$$

where $\langle x \rangle$ and $H(x)$ are McCauley bracket and step function, respectively: when $x \geq 0$, $\langle x \rangle = x$ and $H(x) = 1$; when $x < 0$, $\langle x \rangle = H(x) = 0$. $G_{TRIP}^{\alpha}\left(\xi_{rev}^{\alpha}\right)$ is the generalized force and a function of reversible martensite volume fraction. $T_{TRIP}^{\alpha}\left(\gamma_{TRIP}^{\alpha}\right)$ is the resistance of the α-th friction system. The parameter D_{TRIP} is the reference resistance. The parameter μ_{TRIP} describes the difference between evolution features of TRIP in forward and reverse transformation. As shown in Eqs. (32.b) and (32.c), the parameters $G_{TRIP}^{\alpha}\left(\xi_{rev}^{\alpha}\right)$ and $T_{TRIP}^{\alpha}\left(\gamma_{TRIP}^{\alpha}\right)$ depend on reversible volume fraction of the α-th martensite variant ξ_{rev}^{α} and γ_{TRIP}^{α}, respectively. d_{TRIP} is a material parameter. $H\left(\pi_{TRIP}^{\alpha}\right)$ is used to ensure that $\dot{\gamma}_{TRIP}^{\alpha}$ is always positive and the 2nd law of thermodynamics is satisfied.

2.2.3. Evolution equations for irreversible phase transformation

Since the formation of residual martensite is an irreversible dissipative process, the condition for irreversible martensite volume fraction to satisfy the 2nd law of thermodynamics is:

$$\begin{cases} \dot{\xi}_{ire}^{\alpha} > 0 & \pi_{tr,ire}^{\alpha} \geq 0 \\ \dot{\xi}_{ire}^{\alpha} = 0 & \text{no constraint} \end{cases} \tag{33.a}$$

(33.b)

Using Eqs. (33.a) and (33.b), an evolution law for residual martensite is expressed as (Yu et al., 2013):

$$\dot{\xi}_{ire}^{\alpha} = \left(\left\langle \dot{\xi}_{rev}^{\alpha} \right\rangle + \mu_{ire} \left\langle -\dot{\xi}_{rev}^{\alpha} \right\rangle \right) \left\langle \frac{G_{ire}^{\alpha}\left(\xi_{rev}^{\alpha}\right) - T_{ire}^{\alpha}\left(\xi_{ire}^{\alpha}\right)}{D_{ire}} \right\rangle H\left(\pi_{tr,ire}^{\alpha}\right) \tag{34.a}$$

$$G_{ire}^{\alpha}\left(\xi_{rev}^{\alpha}\right) = \left(\xi_{rev}^{\alpha}\right)^{n} \tag{34.b}$$

$$T_{ire}^{\alpha}\left(\xi_{ire}^{\alpha}\right) = d_{ire}\xi_{ire}^{\alpha} \tag{34.c}$$

where $G_{ire}^{\alpha}\left(\xi_{rev}^{\alpha}\right)$ is the generalized force and $T_{ire}^{\alpha}\left(\xi_{ire}^{\alpha}\right)$ is the resistance of residual martensite. D_{ire} is a reference resistance and μ_{ire} is a material constant. As shown in Eqs. (34.b) and (34.c), $G_{ire}^{\alpha}\left(\xi_{rev}^{\alpha}\right)$ and $T_{ire}^{\alpha}\left(\xi_{ire}^{\alpha}\right)$ are functions of reversible and irreversible parts of martensite variants, respectively. d_{ire} is a material parameter.

2.2.4. Evolution equations for detwinning

Considering Eqs. (26.d) and (27.d) and using a power-law form, an evolution equation for detwinning of the α-th martensite variant is expressed as:

$$\begin{cases} \dot{\lambda}^{\alpha} = \left\langle \frac{\pi_{det}^{\alpha}}{K^{det}} \right\rangle^{n_{det}} \operatorname{sign}\left(\left(\boldsymbol{\sigma} + \mathbf{B}\right) : \mathbf{P}_{det}^{\alpha} \right) & \text{if } \xi^{\alpha} > 0 \\ \dot{\lambda}^{\alpha} = 0 & \text{other conditions} \end{cases} \tag{35.a}$$

(35.b)

where K^{det} is the detwinning resistance and n_{det} represents the rate sensitivity of detwinning.

Although the rate dependent formulation is used, adopting a large value for n_{det}, a rate independent response can be obtained. It should be noted that, depending on the sign of the term $\left(\boldsymbol{\sigma} + \mathbf{B}\right) : \mathbf{P}_{det}^{\alpha}$, the volume fraction of sub-variants can decrease or increase during loading.

2.2.5. Evolution equations for detwinning-induced plasticity

Since DIP is an irreversible dissipative process, $\dot{\gamma}_{DIP}^{\alpha}$ will always be non-negative, i.e., $\dot{\gamma}_{DIP}^{\alpha} \geq 0$.

Therefore, the condition for $\dot{\gamma}_{DIP}^{\alpha}$ to satisfy the 2nd law of thermodynamics is:

$$\begin{cases} \dot{\gamma}_{DIP}^{\alpha} > 0 & \text{if } \pi_{DIP}^{\alpha} \geq 0 \quad (36.a) \\ \dot{\gamma}_{DIP}^{\alpha} = 0 & \text{no constraint} \quad (36.b) \end{cases}$$

According to the experimental observations (Song et al., 2014), the residual and peak strains accumulate during cyclic loading of NiTi and will be saturated after some cycles. Using this fact and Eqs. (24.e), (36.a), and (36.b), an evolution equation for $\dot{\gamma}_{DIP}^{\alpha}$ is proposed here as:

$$\dot{\gamma}_{DIP}^{\alpha} = b_3 \left\langle \gamma_{DIP}^{sat} - \gamma_{DIP}^{\alpha} \right\rangle \left| \dot{\xi}_{rev}^{\alpha} \right| H\left(\pi_{DIP}^{\alpha}\right) \quad (37)$$

where b_3 is a parameter controlling the saturation rate of detwinning-induced plasticity, γ_{DIP}^{sat} is the saturation value of γ_{DIP}. Considering the dissipation inequality for DIP, it is obvious that $\dot{\gamma}_{DIP}^{\alpha}$ and π_{DIP}^{α} should have the same sign. $H\left(\pi_{DIP}^{\alpha}\right)$ ensures that the 2nd law of thermodynamics is satisfied, so that , $\dot{\gamma}_{DIP}^{\alpha}$ >0 if $\pi_{DIP}^{\alpha} > 0$, and $\dot{\gamma}_{DIP}^{\alpha} = 0$ if $\pi_{DIP}^{\alpha} \leq 0$. According to Eq. (26.e), as most of the components of $\mathbf{P}_{det}^{\alpha}$ are negative, a positive value of π_{DIP}^{α} is more probable in compressive loading, whereas a negative value is more probable in tensile loading. Therefore, using $H\left(\pi_{DIP}^{\alpha}\right)$ in Eq. (37) causes $\dot{\gamma}_{DIP}^{\alpha}$, and subsequently the DIP strain $\boldsymbol{\varepsilon}^{DIP}$, to be zero in tension. A summary of the proposed constitutive model at the single crystal scale is presented in Table 1.

Table 1: Summary of the proposed constitutive model

$\boldsymbol{\varepsilon} = \boldsymbol{\varepsilon}^{e} + \boldsymbol{\varepsilon}^{in}$	Strain decomposition
$\boldsymbol{\varepsilon}^{in} = \boldsymbol{\varepsilon}^{tr} + \boldsymbol{\varepsilon}^{TRIP} + \boldsymbol{\varepsilon}^{det} + \boldsymbol{\varepsilon}^{DIP}$	
$\boldsymbol{\varepsilon}^{tr} = \sum_{\alpha=1}^{24} \xi_{rev}^{\alpha} g^{tr} \mathbf{P}^{\alpha} + \sum_{\alpha=1}^{24} \xi_{ire}^{\alpha} g^{tr} \mathbf{P}^{\alpha}$	
$\boldsymbol{\varepsilon}^{TRIP} = \sum_{\alpha=1}^{24} \gamma_{TRIP}^{\alpha} \mathbf{P}^{\alpha}$	
$\boldsymbol{\varepsilon}^{det} = \sum_{\alpha=1}^{24} \xi^{\alpha} \left(\lambda^{\alpha} - \lambda_0^{\alpha}\right) \mathbf{P}_{det}^{\alpha}$	
$\boldsymbol{\varepsilon}^{DIP} = \sum_{\alpha=1}^{24} \gamma_{DIP}^{\alpha} \mathbf{P}_{det}^{\alpha}$	
$\pi_{tr,rev}^{\alpha} = (\boldsymbol{\sigma} + \mathbf{B}) : \left(g^{tr} \mathbf{P}^{\alpha} + \left(\lambda^{\alpha} - \lambda_0^{\alpha}\right) \mathbf{P}_{det}^{\alpha}\right) - \beta\left(T - T_0\right) - \mathrm{X}^{\alpha}$	Thermodynamic deriving forces

$$\pi^{\alpha}_{tr,ire} = \left(\boldsymbol{\sigma}+\mathbf{B}\right):\left(g^{tr}\mathbf{P}^{\alpha}+\left(\lambda^{\alpha}-\lambda^{\alpha}_{0}\right)\mathbf{P}^{\alpha}_{det}\right)-\beta\left(T-T_{0}\right)$$

$$\pi^{\alpha}_{TRIP} = \left(\boldsymbol{\sigma}+\mathbf{B}\right):\mathbf{P}^{\alpha}$$

$$\pi^{\alpha}_{det} = \left|\left(\boldsymbol{\sigma}+\mathbf{B}\right):\xi^{\alpha}\mathbf{P}^{\alpha}_{det}\right|-\mathrm{X}^{\alpha}_{\mathrm{det}}$$

$$\pi^{\alpha}_{DIP} = \left(\boldsymbol{\sigma}+\mathbf{B}\right):\mathbf{P}^{\alpha}_{det}$$

$$\begin{cases} \dot{\xi}^{\alpha}_{rev} = \left|\dfrac{\pi^{\alpha}_{tr,rev}}{Y}\right|^{n_{tr}} & \text{if } \left(\pi^{\alpha}_{tr,rev}>0,\quad \xi^{\alpha}<1,\quad \xi<1\right) \\ \dot{\xi}^{\alpha}_{rev} = -\left|\dfrac{\pi^{\alpha}_{tr,rev}}{K^{tr}}\right|^{n_{tr}} & \text{if } \left(\pi^{\alpha}_{tr,rev}<0,\quad \xi^{\alpha}>\xi^{\alpha}_{ire},\quad \xi>\xi_{ire}\right) \\ \dot{\xi}^{\alpha}_{rev} = 0 & \text{other conditions} \end{cases}$$

Evolution equations for reversible phase transformation

$$\dot{\xi}^{\alpha}_{ire} = \left(\left\langle\dot{\xi}^{\alpha}_{rev}\right\rangle+\mu_{ire}\left\langle-\dot{\xi}^{\alpha}_{rev}\right\rangle\right)\left\langle\frac{G^{\alpha}_{ire}\left(\xi^{\alpha}_{rev}\right)-T^{\alpha}_{ire}\left(\xi^{\alpha}_{ire}\right)}{D_{ire}}\right\rangle H\left(\pi^{\alpha}_{tr,ire}\right)$$

Evolution equation for residual martensite

$$\dot{\gamma}^{\alpha}_{TRIP} = \left(\left\langle\dot{\xi}^{\alpha}_{rev}\right\rangle+\mu_{TRIP}\left\langle-\dot{\xi}^{\alpha}_{rev}\right\rangle\right)\left\langle\frac{G^{\alpha}_{TRIP}\left(\xi^{\alpha}_{rev}\right)-T^{\alpha}_{TRIP}\left(\gamma^{\alpha}_{TRIP}\right)}{D_{TRIP}}\right\rangle H\left(\pi^{\alpha}_{TRIP}\right)$$

Evolution equation for transformation-induced plasticity

$$\begin{cases} \dot{\lambda}^{\alpha} = \left\langle\dfrac{\pi^{\alpha}_{det}}{K^{det}}\right\rangle^{n_{det}}\mathrm{sign}\left(\left(\boldsymbol{\sigma}+\mathbf{B}\right):\mathbf{P}^{\alpha}_{det}\right) & \text{if } \xi^{\alpha}>0 \\ \dot{\lambda}^{\alpha} = 0 & \text{other conditions} \end{cases}$$

Evolution equations for detwinning

$$\dot{\gamma}^{\alpha}_{DIP} = b_{3}\left\langle\gamma^{sat}_{DIP}-\gamma^{\alpha}_{DIP}\right\rangle\left|\dot{\xi}^{\alpha}_{rev}\right|H\left(\pi^{\alpha}_{DIP}\right)$$

Evolution equation for detwinning-induced plasticity

2.3. Explicit scale-transition rule

To transform the single crystal response into polycrystalline version, an explicit scale-transition rule (Yu et al., 2013) is used in this work. In comparison to implicit self-consistent modelling approach proposed by Hill (1965), the explicit scale-transition approach proposed by Kröner (1961) leads to a convenient "a priori" interaction law that facilitates easy application and comparison with experimental results. In Kröner's model, each crystal of the polycrystalline material is treated as an inclusion inside a matrix which is made from other crystals of the material. This approach is based on the assumption of elastic interaction between the matrix and the inclusion. An extension of this model by Berveiller and Zaoui (1978) allows for elasto-plastic intergranular accommodation and plastic internal stress relaxation. The method of Berveiller and Zaoui has previously been used to describe ratchetting of polycrystalline materials (Cailletaud and Sai, 2008; Kang et al., 2011). It has also been adopted to describe the thermo-mechanical properties

of NiTi shape memory alloys (SMAs) (Yu et al., 2014; Yu et al., 2013; Yu et al., 2012, 2015). With the assumption of uniform isotropic elasticity for the polycrystalline aggregates, the relation between stress tensor in a single crystal $\boldsymbol{\sigma}$ and the applied uniform macroscopic stress tensor $\boldsymbol{\Sigma}$ can be expressed by:

$$\boldsymbol{\sigma} = \boldsymbol{\Sigma} + D\left(\mathbf{E}^{in} - \boldsymbol{\varepsilon}^{in}\right) \tag{38}$$

where $\mathbf{E}^{in} = \left[\boldsymbol{\varepsilon}^{in}\right]$ is the inelastic strain of polycrystalline aggregates obtained by the volume average of each single crystal strain tensor. The symbol $[\bullet]$ denotes the volume average over the entire grains in a polycrystalline aggregate. D is a material parameter reflecting the heterogeneity of stress field at the inter-granular scale. The value of D can be set to a value between zero and $\frac{4G\left(4-5\nu\right)}{15\left(1-\nu\right)}$ where G is the shear modulus of the material and ν is the Poisson's ratio. If $D = 0$ the heterogeneity at the intergranular scale is neglected and a uniform stress field is obtained in the entire polycrystalline aggregates. As the value of D is increased, the heterogeneity of the polycrystalline material is increased.

3. Material parameters identification

Since the response of NiTi shape memory alloy is rate-independent and viscosity is not significant, the parameters n_{tr} and n_{det} are set to be sufficiently large so that material behavior is effectively rate independent. The parameter β controls the start-stress of forward transformation at a specific temperature and can be calibrated by fitting the curves related to the start-stress of transformation at different temperatures. Since the elastic constants for monoclinic single crystal martensite in NiTi SMA are not available, we assume the elastic modulus to be isotropic. As we are focusing on inelastic response of shape memory alloys, the elastic modulus is considered the same for austenite and martensite phases. The Poisson's ratio is based on the study of Thamburaja (2005).

Two different parameters, Y and K^{tr} are adopted to describe the evolution law of reversible martensite volume fraction during forward and reverse transformation. Both parameters control the width of hysteresis loop. Parameters Y_0 and Y_d control the width of hysteresis loop during forward transformation in the first and steady-state cycles, respectively. The role of K^{tr} is to control the width of hysteresis loop during reverse transformation. The parameters $\mathrm{h}_{\mathrm{det}}$ and $\mathrm{K}^{\mathrm{det}}$

can be obtained by fitting the curves related to detwinning modulus and start-stress of detwinning, respectively.

As commented by Liu et al. (1998), the effect of DIP is not obvious during tensile loading. On the other hand, Kang et al. (2009) commented that the accumulated peak strain during uniaxial cyclic deformation is mainly caused by transformation-induced plasticity while the accumulated residual strain comes from both the transformation-induced plasticity and residual martensite. Thus, the parameters n, D_{TRIP}, d_{TRIP}, and μ_{TRIP} can be obtained from the data of accumulated peak strain in tensile cyclic loading. The parameters d_{ire}, D_{ire}, and μ_{ire} can be measured by fitting to the data related to the difference of peak and residual strains in tensile cyclic loading.

The parameter b_3 controls the saturation rate of detwinning-induced plasticity and γ_{DIP}^{sat} is the saturated value of detwinning-induced plasticity. These parameters are calibrated by fitting the evolution curves of residual strain under compressive loading. The parameters H_0 and H_{sat} control transformation hardening and can be calibrated by measuring transformation modulus at the first and steady-state cycles, respectively. The fact that the start-stress of martensite transformation decreases with increasing number of cycles is taken into account by using B_{sat}. This parameter can be obtained by measuring the start-stress of martensite transformation in the first and steady-state cycles. Parameters b_1 and b_2 control the saturation rates of $\|\mathbf{B}^{\alpha}\|$ and H^{α}, respectively. They can be calibrated by fitting the evolution curves of decreased start-stress of martensite transformation and hardening modulus, respectively. The parameter g^{tr} controls the maximum transformation strain and can be calibrated from the measured value of transformation strain. The value of the parameter D in the scale-transition rule is set to be the same as that used by Yu et al. (2015). It should be noted that since all parameters are related to a single crystal, they should ideally be obtained from stress-strain curves of a single crystal. As the experimental data for single crystal is not available, the parameters are calibrated by a trial-and-error method from polycrystalline experimental data.

In order to explore the predictive capability of the proposed constitutive model, two sets of experimental test data are considered (Kang et al., 2009; Yu et al., 2013). Both experimental tests entail cyclic loading of super-elastic NiTi SMA with 50.2 at.% Ni. The finish-temperature of austenite for this alloy is 268 K. The original phase of the material is austenite, given that both tests are performed at room temperature. In the experiments of Kang et al. (2009) stress-controlled

cyclic loading regimes are applied to the SMA, including tension-compression tests and tension-unloading tests. In the experiments of Yu et al. (2013) strain-controlled cyclic loading regimes are applied to the SMA, including compression-unloading tests and tension-unloading tests. The stress-controlled cyclic tests, up to 160 cycles, are related to tension-compression tests with two mean stresses of 100 MPa and 0 MPa, and stress amplitudes of ±450 MPa, as well as tension-unloading tests with peak stress of 550 MPa. The strain-controlled cyclic tests, up to 50 cycles, are related to compression-unloading tests with two minimum strains of -2.5% and -3.5%, and cyclic tension-unloading tests with peak strain of 3.5%.

The calibrated parameters used in this study are listed in Table 2.

Table 2: Material parameters used in the prediction of cyclic loading considering DIP

Parameter	Symbol	Value	Unit
Young's modulus	E	72	GPa
A constant controlling the start-stress of forward transformation	β	0.733	MJ/K
Poisson's ratio	ν	0.3	-
The martensite start-temperature	M_{0s}	265	K
Constants controlling the rate sensitivity of martensite transformation and detwinning, respectively	n_{tr} , $n_{\det}$	30 , 30	-
Saturation value of internal stress	B_{sat}	50	MPa
The initial value of Y , a constant controlling the dependence of Y on the current martensite volume fraction	Y_0 , Y_d	4 , 5	MPa
A constant controlling the evolution law of martensite volume fraction during reverse transformation	K^{tr}	25	MPa
Initial and saturation values of hardening modulus	H_0 , H_{sat}	80 , 400	MPa
A constant controlling the dependence of TRIP and residual martensite on the applied stress	n	3	-
Reference resistance for TRIP, a constant controlling the resistance of the α-th friction system	D_{TRIP} , d_{TRIP}	3.5e-3 , 5e-3	-
Reference resistance for residual martensite, a constant controlling the resistance of residual martensite	D_{ire} , d_{ire}	1e-3 , 1e-3	-
Constants describing the difference between evolution features in forward and reverse transformations	μ_{TRIP} , μ_{ire}	0.2	-

Constants controlling saturation rate of internal stress, evolution rate of hardening modulus, and saturation rate of DIP, respectively	b_1, b_2, b_3	2, 2, 1	-
Hardening modulus for detwinning, detwinning resistance	h_{det}, K^{det}	1000, 20	MPa
The saturation value of shearing deformation caused by DIP	γ_{DIP}^{sat}	0.05	-
A constant reflecting the heterogeneity of stress field in the inter-granular scale	D	2	GPa

4. Results and discussion

In this section we first establish the role of texture on tension-compression asymmetry in our modeling framework. We then investigate the role of DIP in cyclic tension and compression loading conditions.

4.1. Influence of texture on asymmetry in a single loading cycle

Depending on manufacturing process, polycrystalline shape memory alloys can have a strong texture (Thamburaja and Anand, 2001). Since the samples used in the experiments are manufactured from extruded solid bars, the texture formed in the process of extrusion will affect the polycrystalline response of the material. Based on the method used for forming NiTi shape memory alloys, three different textures with different effects on the overall response of the alloy can be formed: a $[100]$ texture with stiffer mechanical response in tension than in compression, a $[111]$ texture with softer response in tension than in compression, and a $[110]$ texture with almost no effect on the mechanical responses in tension or compression (Gall et al., 2001).

In order to show the effect of texture on asymmetrical response of shape memory alloys, 40 single crystals in the 3 aforementioned textures are considered. Employing rotation matrix in three dimensions, Euler angles for each of 40 crystals are selected such that a specific direction of all grains is aligned with the loading direction. Predicted differences between stress-strain curves in tension and compression for different textures are shown in Fig. 1. For randomly oriented grains, grains with $[100]$ texture, and grains with $[110]$ texture, more hardening occurs in tension than in

compression, although the difference is not pronounced for the $[110]$ and random textures. In contrast, the $[111]$ texture results in more hardening in compression than in tension.

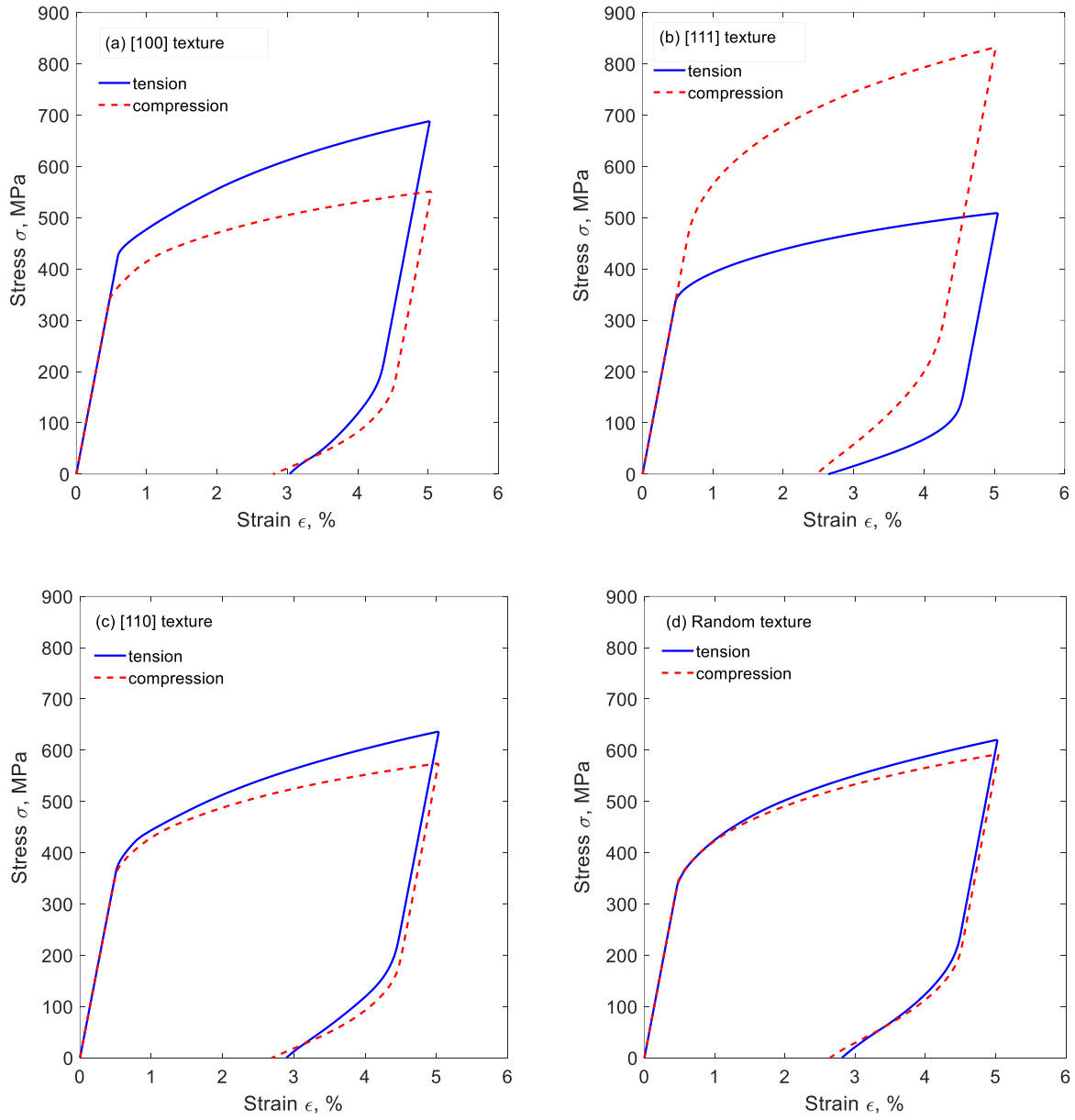

Fig. 1. Stress-strain curves of NiTi shape memory alloy subjected to strain-controlled tension-unloading for different textures: (a) $[100]$ texture, (b) $[111]$ texture, (c) $[110]$ texture, (d) random texture.

4.2. Influence of DIP in cyclic loading

Based on the asymmetrical tension/compression responses observed in the experimental tests of Kang et al. (2009) and Yu et al. (2013), 40 single crystals with $[111]$ texture are adopted to model the behavior of NiTi SMA in this work. To model the $[111]$ texture, the rotation matrix between local coordinate system at a single crystal and global coordinate system at a polycrystalline material is calculated such that the $[111]$ direction of each grain is aligned with the loading direction.

Before presenting comparisons of model predictions with reported experimental data, we first present a sensitivity analysis of the effect of parameters b_3 (controlling the saturation rate of detwinning-induced plasticity) and γ_{DIP}^{sat} (the saturation value of shearing deformation caused by detwinning-induced plasticity) on the computed stress-strain response, as shown in Fig. 2. Computed stress-strain loops for the 20th cycle of stress-controlled tension-compression loading of a single crystal NiTi are shown. As most of the components of $\mathbf{P}_{det}^{\alpha}$ have negative values, a decrease of either b_3 or γ_{DIP}^{sat} results in less negative values of DIP. Therefore, the computed strain throughout the loading cycle increases.

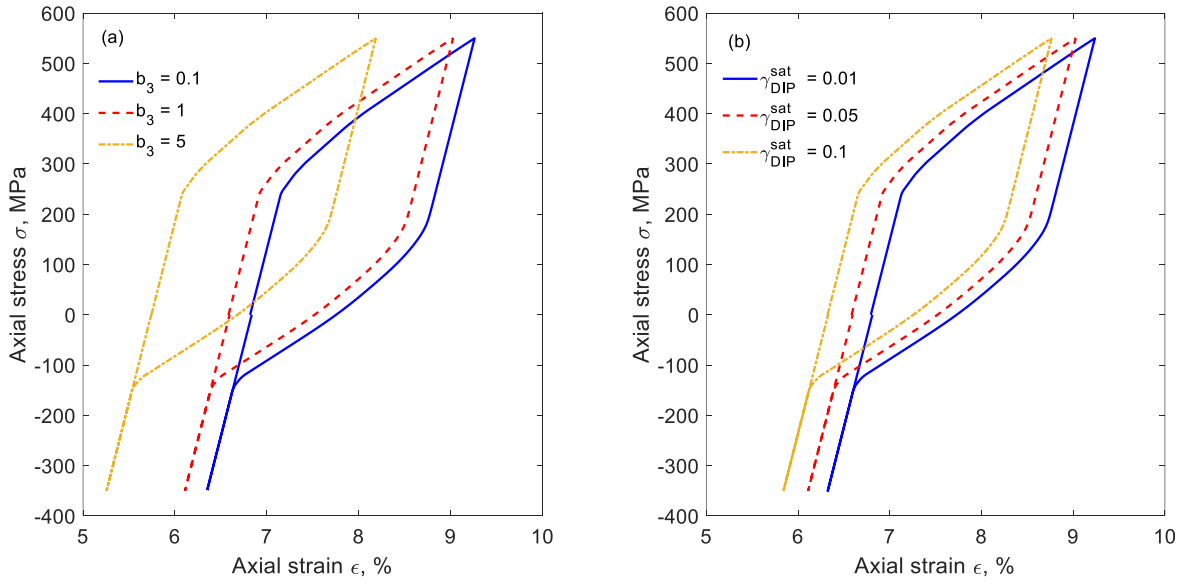

Fig. 2. Effect of parameters (a) b_3 (controlling the saturation rate of DIP) and (b) γ_{DIP}^{sat} (the saturation value of shearing deformation caused by DIP) on stress-strain curves of a single crystal in the 20th cycle for a loading case with a mean stress of 100 MPa and a stress amplitude of ± 450 MPa.

Comparisons between model predictions and the stress-controlled cyclic loading experiments of Kang et al. (2009) are next presented. Model parameters are listed in Table 2. In Fig. 3 we consider the case of applied mean stresses of 100 MPa, with stress amplitudes of ± 450 MPa. In the first cycle, DIP affects the part of the cycle with negative stress very slightly, but this effect becomes more pronounced in subsequent cycles.

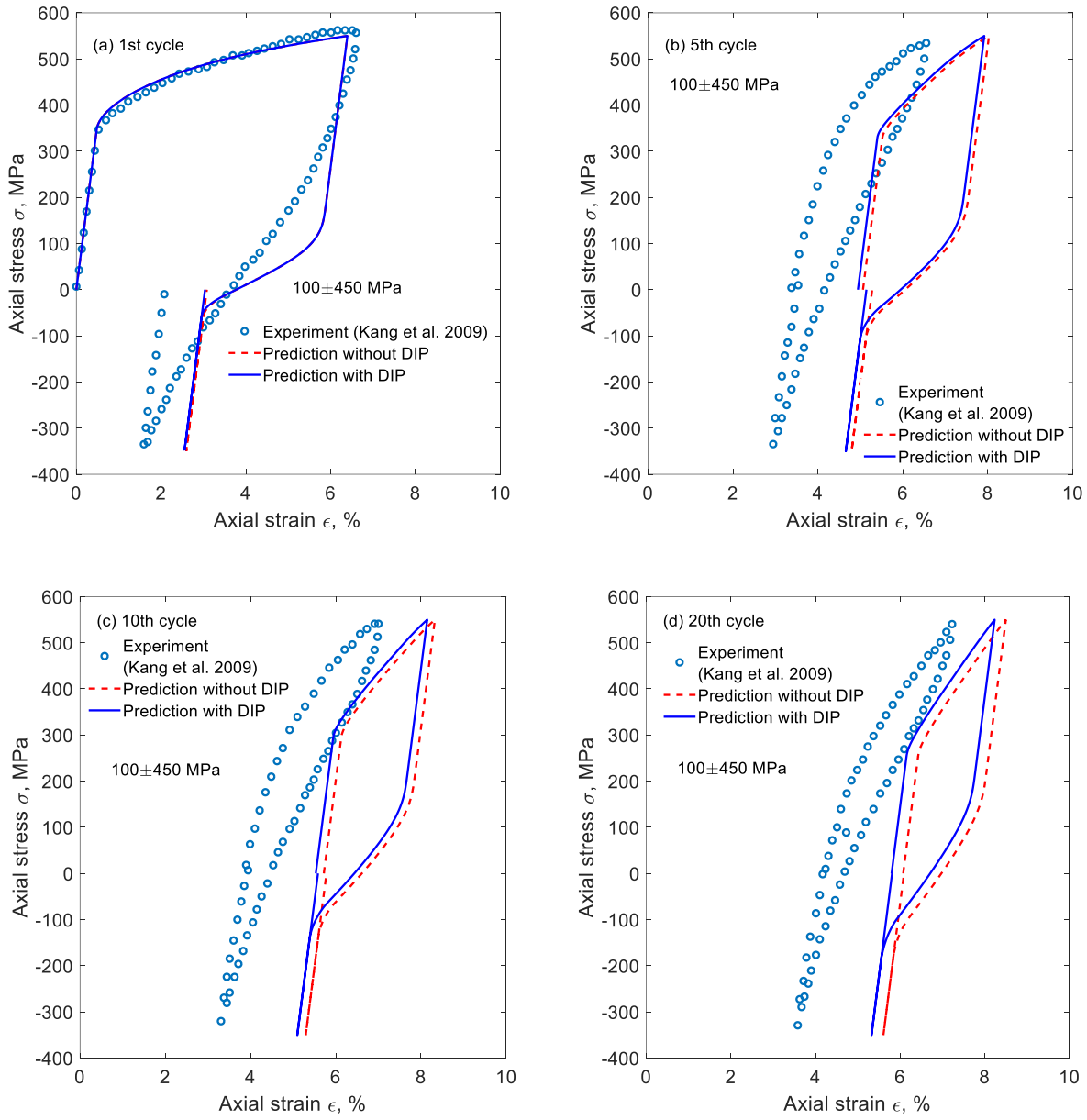

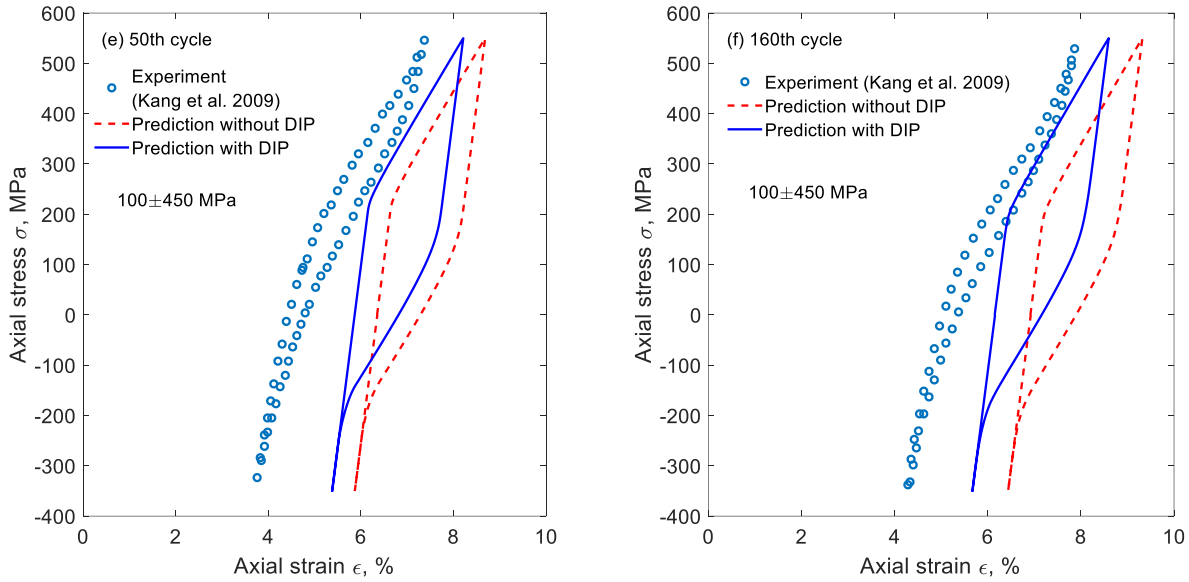

Fig. 3. Experimental and predicted stress-strain curves for stress-controlled cyclic tension-compression tests with a mean stress of 100 MPa and a stress amplitude of ± 450 MPa (100 ± 450 MPa): (a) 1st cycle, (b) 5th cycle, (c) 10th cycle, (d) 20th cycle, (e) 50th cycle, (f) 160th cycle.

The corresponding curves of residual strain, peak strain, and dissipation energy as a function of number of cycles are shown in Fig. 4. In stress-controlled cyclic loadings DIP causes a reduction in both peak strain and residual strain.

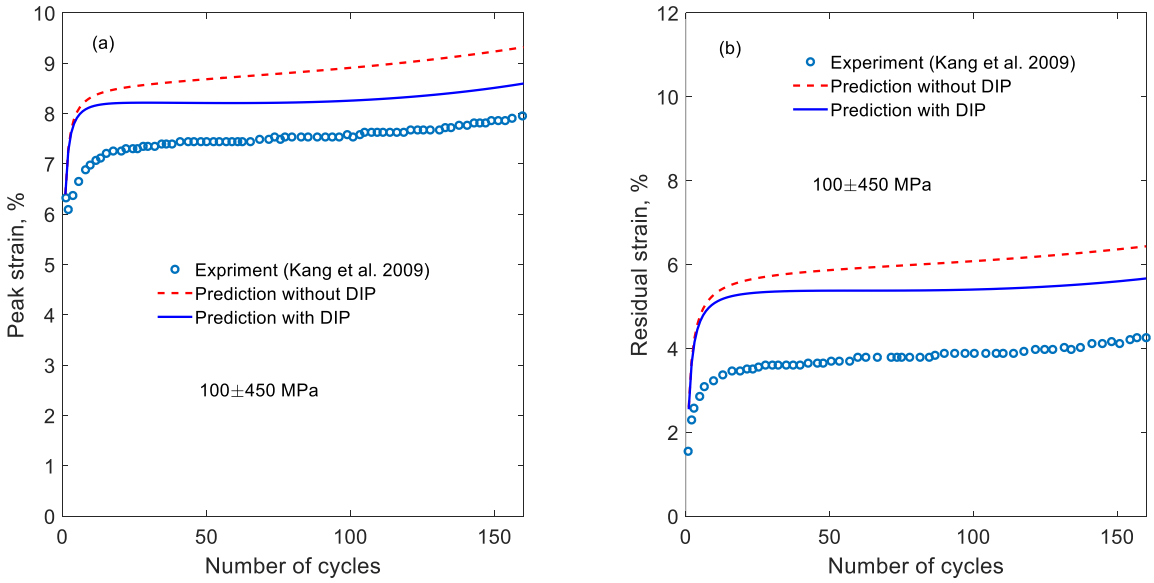

Fig. 4. Experimental and predicted curves for stress-controlled cyclic tension-compression tests with a mean stress of 100 MPa and a stress amplitude of ± 450 MPa: (a) peak strain vs. number of cycles, (b) residual strain vs. number of cycles.

Predicted and experimental stress-strain curves for the loading case with zero mean stress and a stress amplitude of ± 450 MPa are shown in Fig. 5. As the density of dislocations increases during cyclic loading, the effect of DIP becomes more pronounced with increasing cycles. Fig. 6 shows a reduction in both residual and peak strains due to DIP.

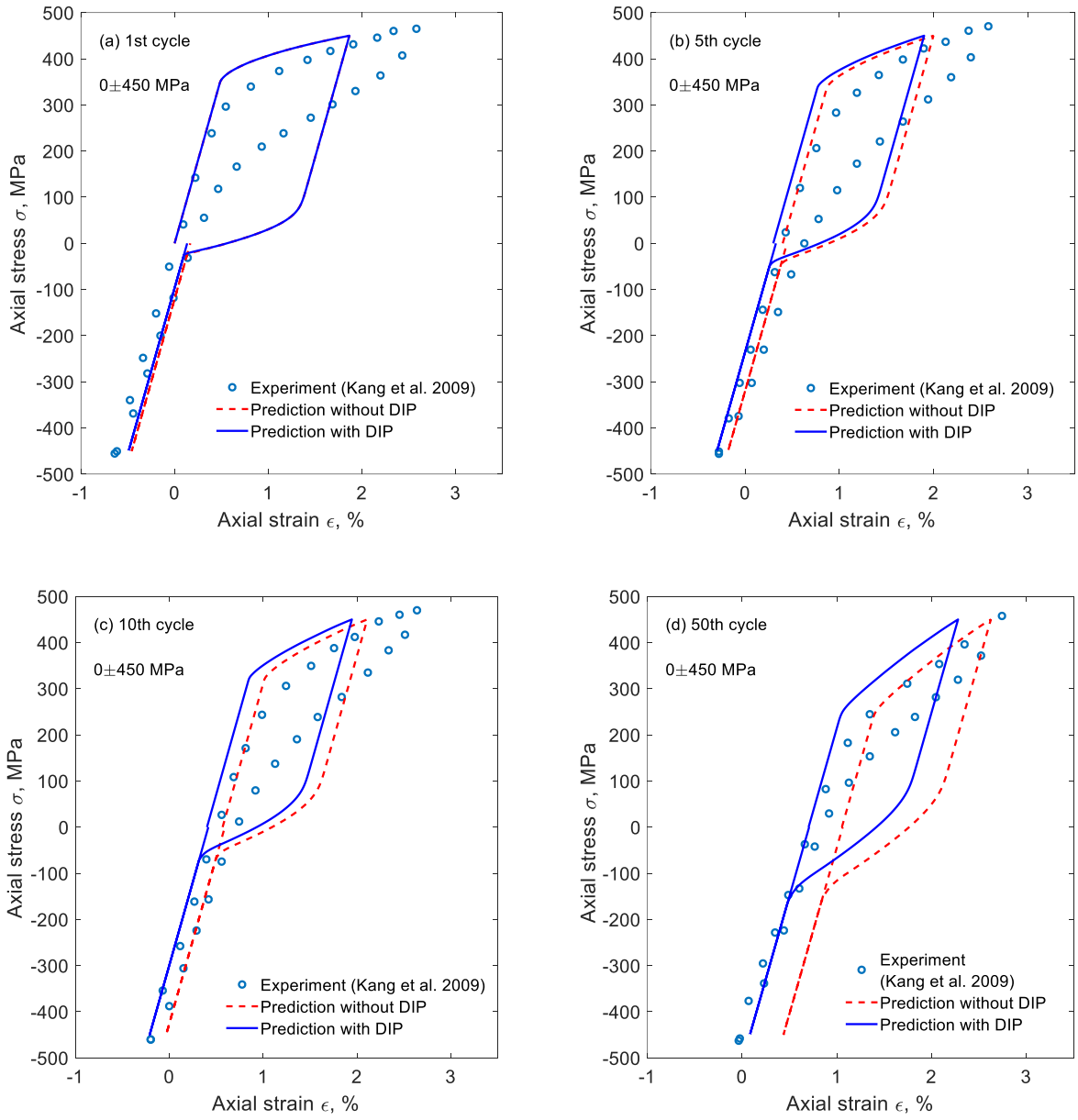

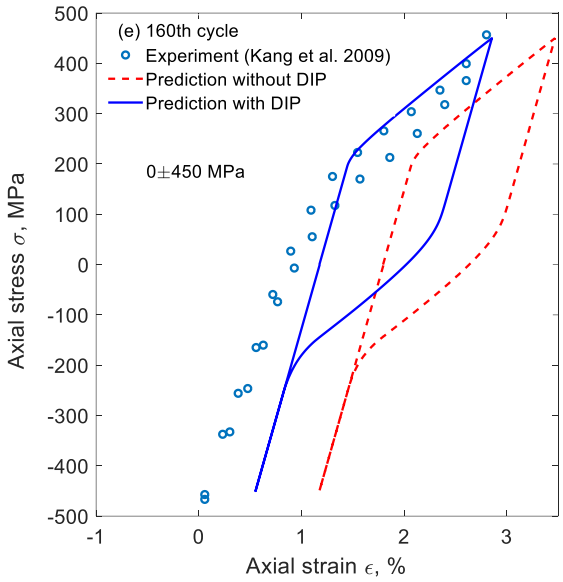

Fig. 5. Experimental and predicted stress-strain curves for stress-controlled cyclic tension-compression tests with zero mean stress and a stress amplitude of ± 450 MPa (0 ± 450 MPa): (a) 1st cycle, (b) 5th cycle, (c) 10th cycle, (d) 50th cycle, (e) 160th cycle.

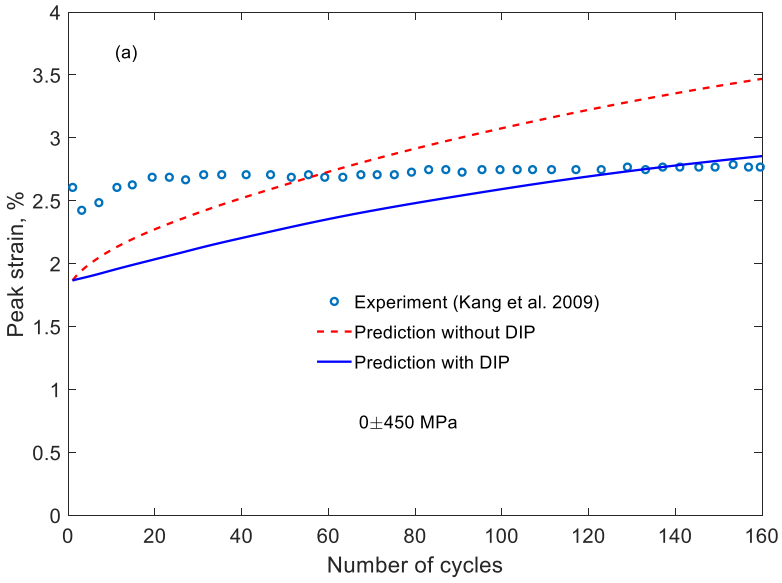

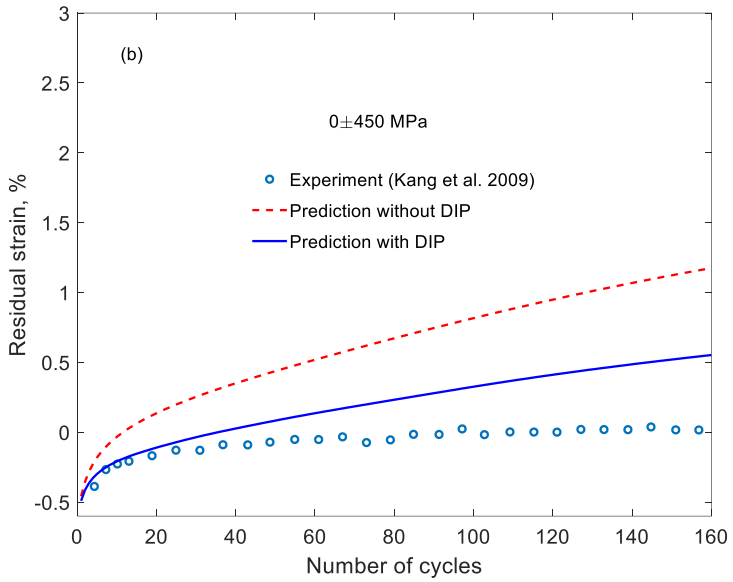

Fig. 6. Experimental and predicted curves for stress-controlled cyclic tension-compression tests with zero mean stress and a stress amplitude of ±450 MPa: (a) peak strain vs. number of cycles, (b) residual strain vs. number of cycles.

Fig. 7 shows the predicted and experimental curves for stress-controlled tensile-unloading cycles, where the applied stress cycles between a maximum value of 550 MPa and a minimum value of 0 MPa. As shown in Fig. 7, DIP does not contribute if compressive stress is not generated during part, or all, of the loading cycle.

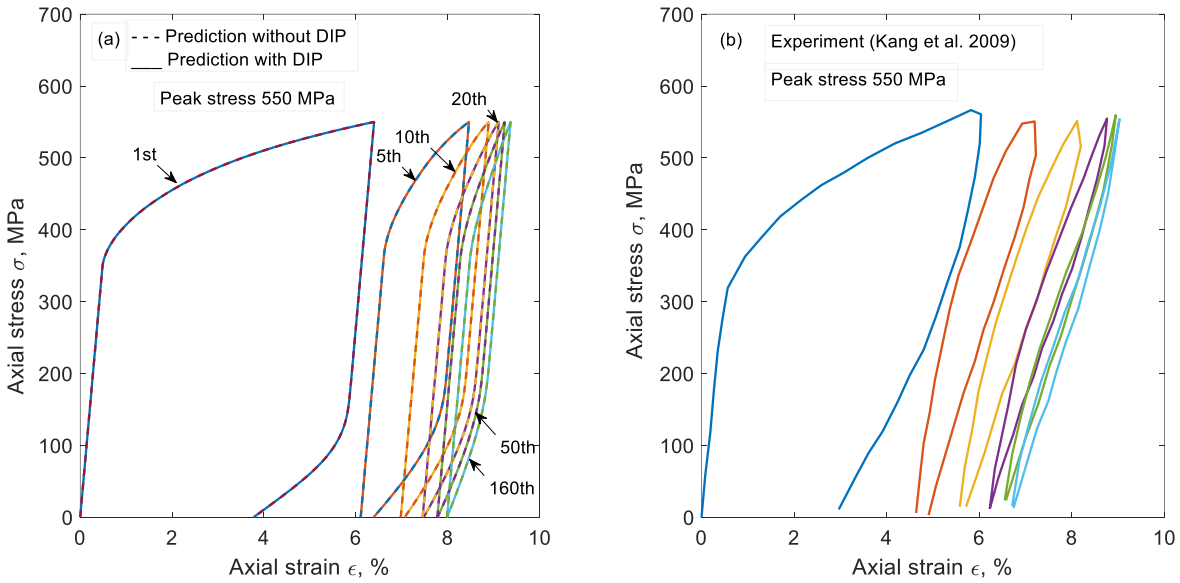

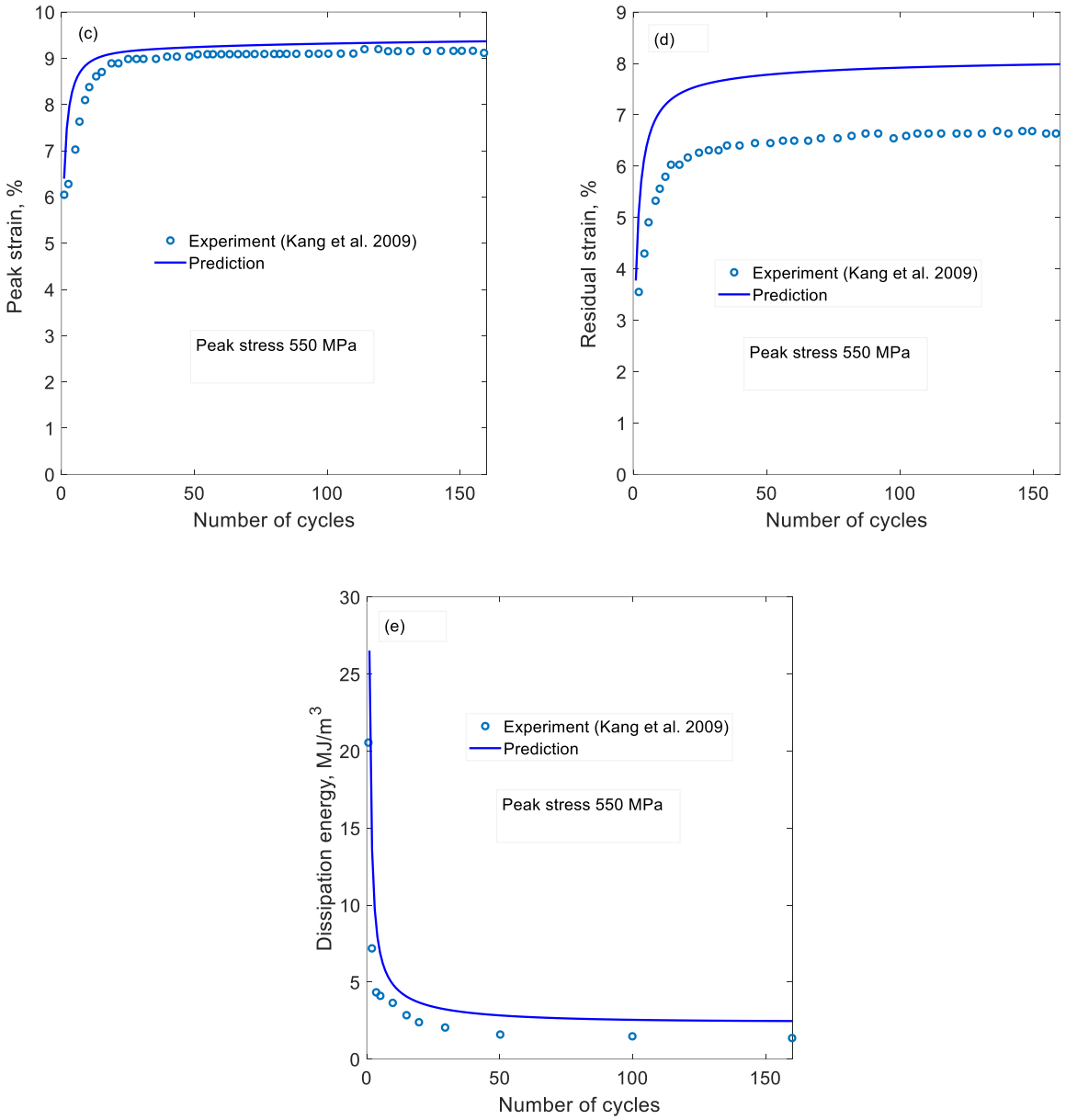

Fig. 7. Experimental and predicted curves for stress-controlled cyclic tension-unloading tests, where the applied stress cycles between a minimum value of 0 MPa and a maximum value of 550 MPa: (a) simulated stress-strain curves, where dashed and solid lines represent simulation without and with considering DIP, respectively, (b) experimental stress-strain curves, (c) peak strain vs. number of cycles, (d) residual strain vs. number of cycles, (e) dissipation energy vs. number of cycles.

Model predictions are next presented for the strain-controlled experiments of Yu et al. (2013). The set of model parameters listed in Table 2 is once again used, as the same polycrystalline NiTi SMA alloy used in the strain-controlled experiments of Yu et al. (2013) and the stress-controlled experiments of Kang et al. (2009) presented above. Fig. 8 shows stress-strain curves for cyclic compression-unloading with a maximum applied strain of 0% and a minimum applied strain of -

2.5%. The effect of DIP is not significant in the 1st cycle but it becomes significant from 2nd cycle onwards. The incorporation of DIP provides improved predictions of the experimental results of Yu et al. (2013), with lower peak compressive stress and higher residual compressive strain.

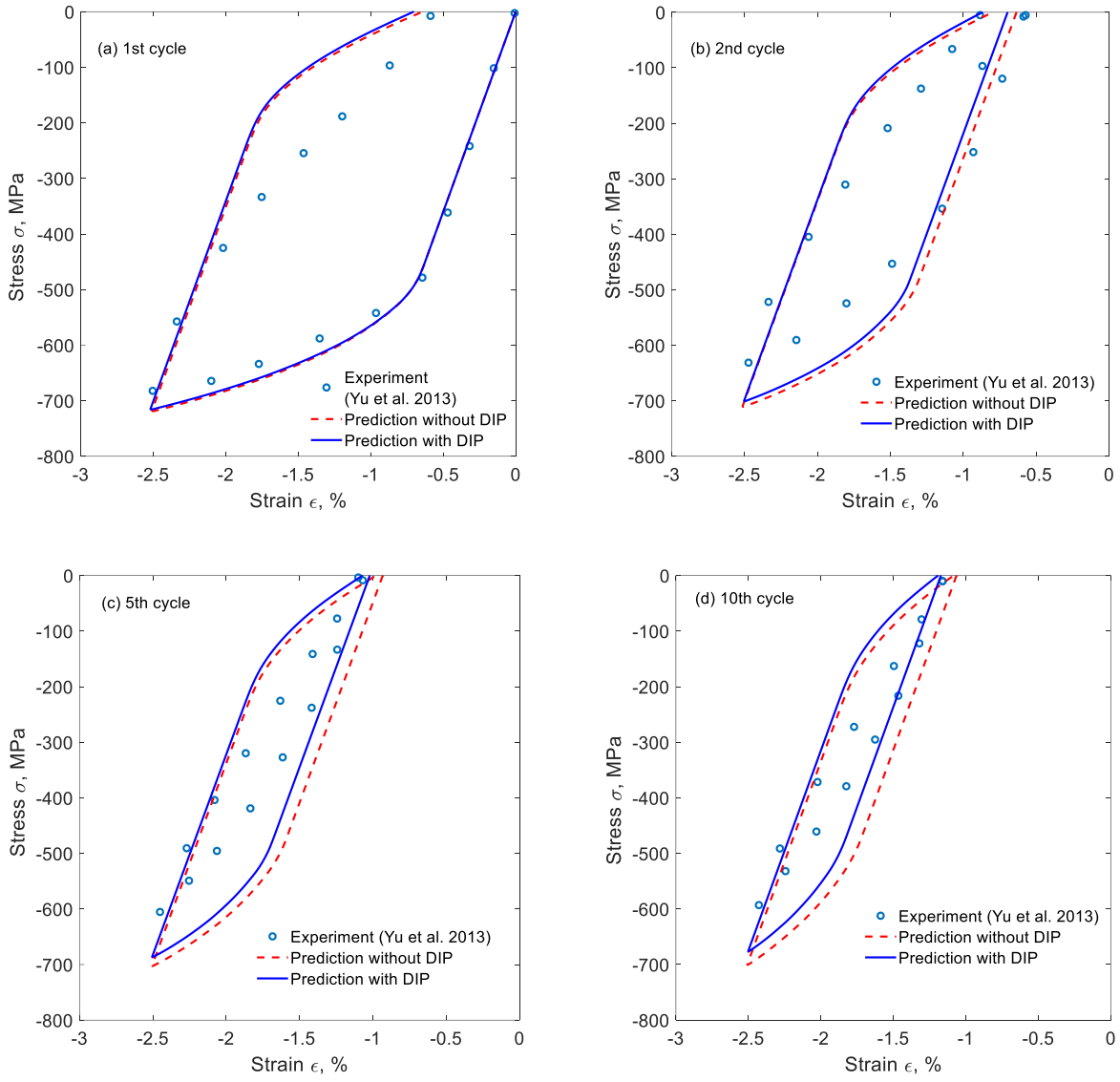

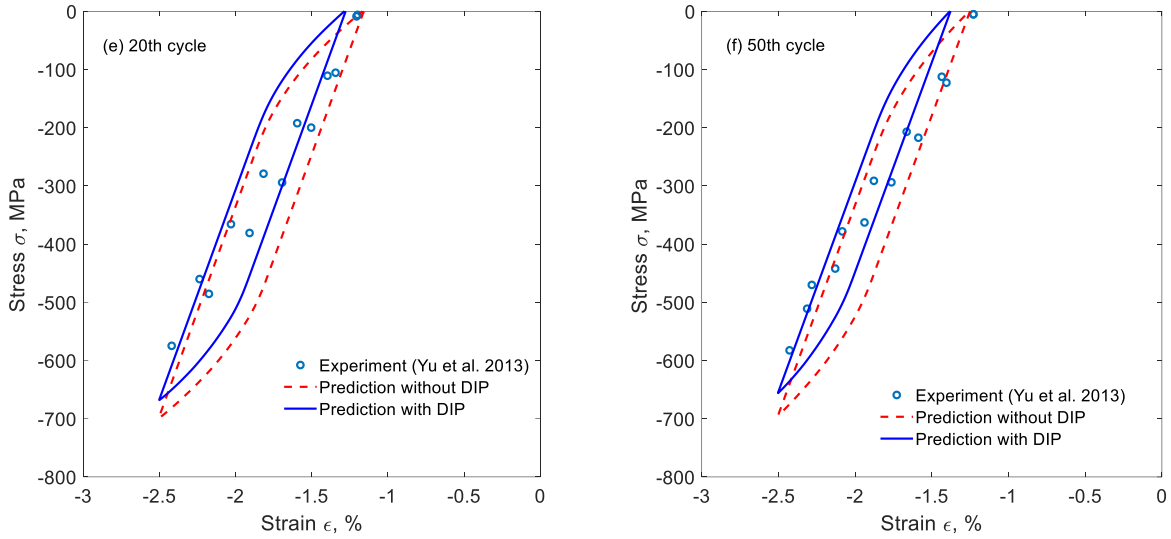

Fig. 8. Experimental and predicted stress-strain curves for strain-controlled cyclic compression-unloading tests where the applied strain cycles between a minimum value of -2.5% and a maximum value of 0%: (a) 1st cycle, (b) 2nd cycle, (c) 5th cycle, (d) 10th cycle, (e) 20th cycle, (f) 50th cycle.

Dissipated energy over 50 loading cycles is shown in Fig. 9(a). Again, the inclusion of DIP in the model provides an improved prediction of the experimental data. DIP also provides an improved prediction of the evolution of peak compressive stress over 50 loading cycles, as shown in Fig. 9(b).

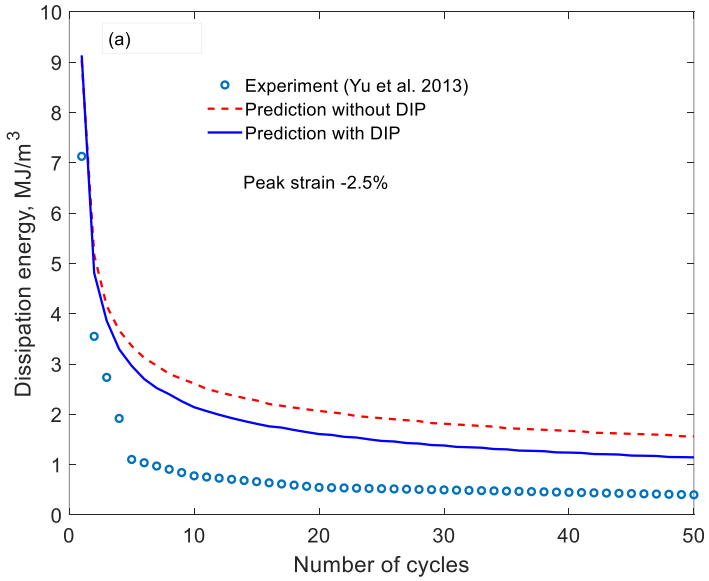

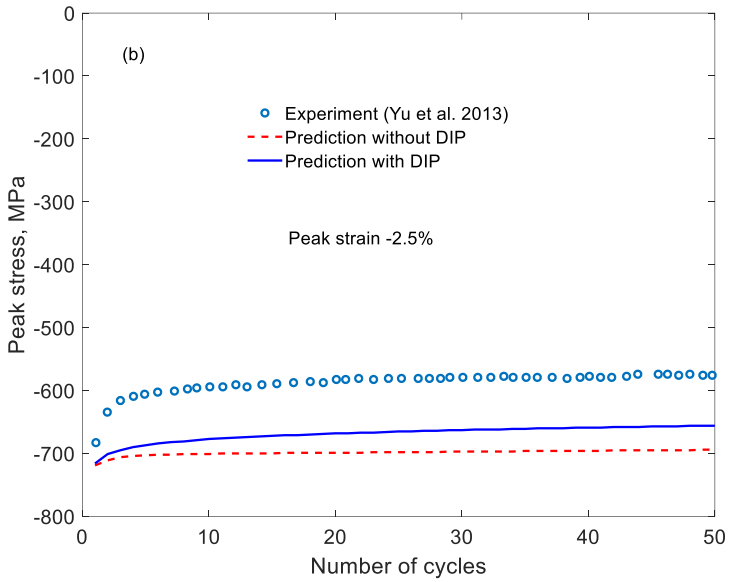

Fig. 9. Experimental and predicted curves for strain-controlled cyclic compression-unloading tests where the applied strain cycles between a minimum value of -2.5% and a maximum value of 0%: (a) dissipation energy vs. number of cycles, (b) peak stress vs. number of cycles.

Fig. 10 shows stress-strain curves for cyclic compression-unloading with a maximum applied strain of 0% and a minimum applied strain of -3.5%. Again, the effect of DIP is not significant in the 1st cycle but it becomes significant from 2nd cycle onwards. As shown in Fig. 11, similar to the case of a minimum applied strain of -2.5%, DIP also provides improved predictions of experimentally measured dissipated energy and peak stress for the higher applied compressive strain of -3.5%.

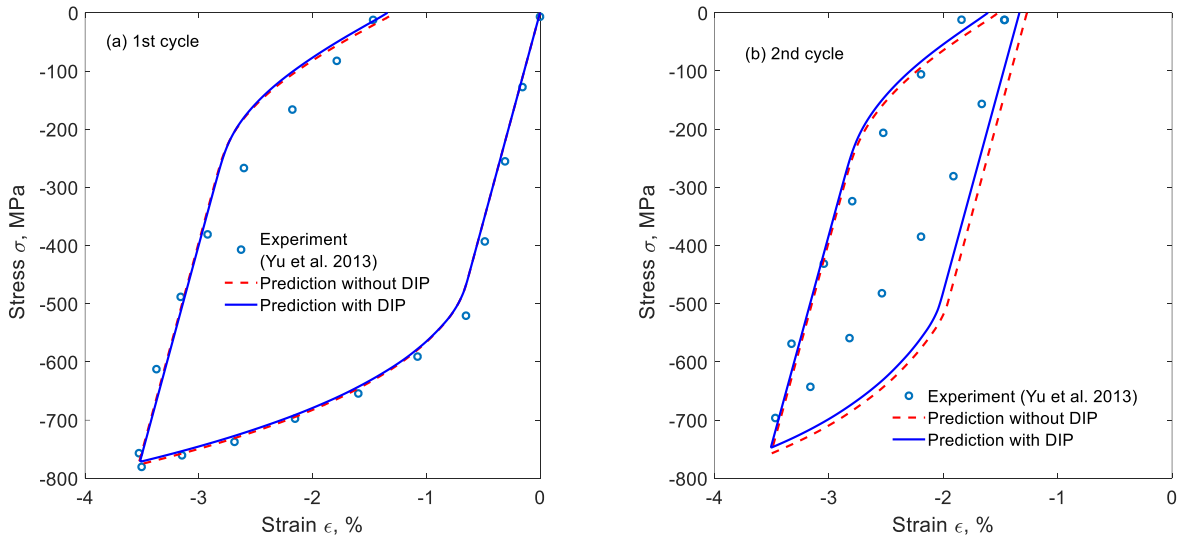

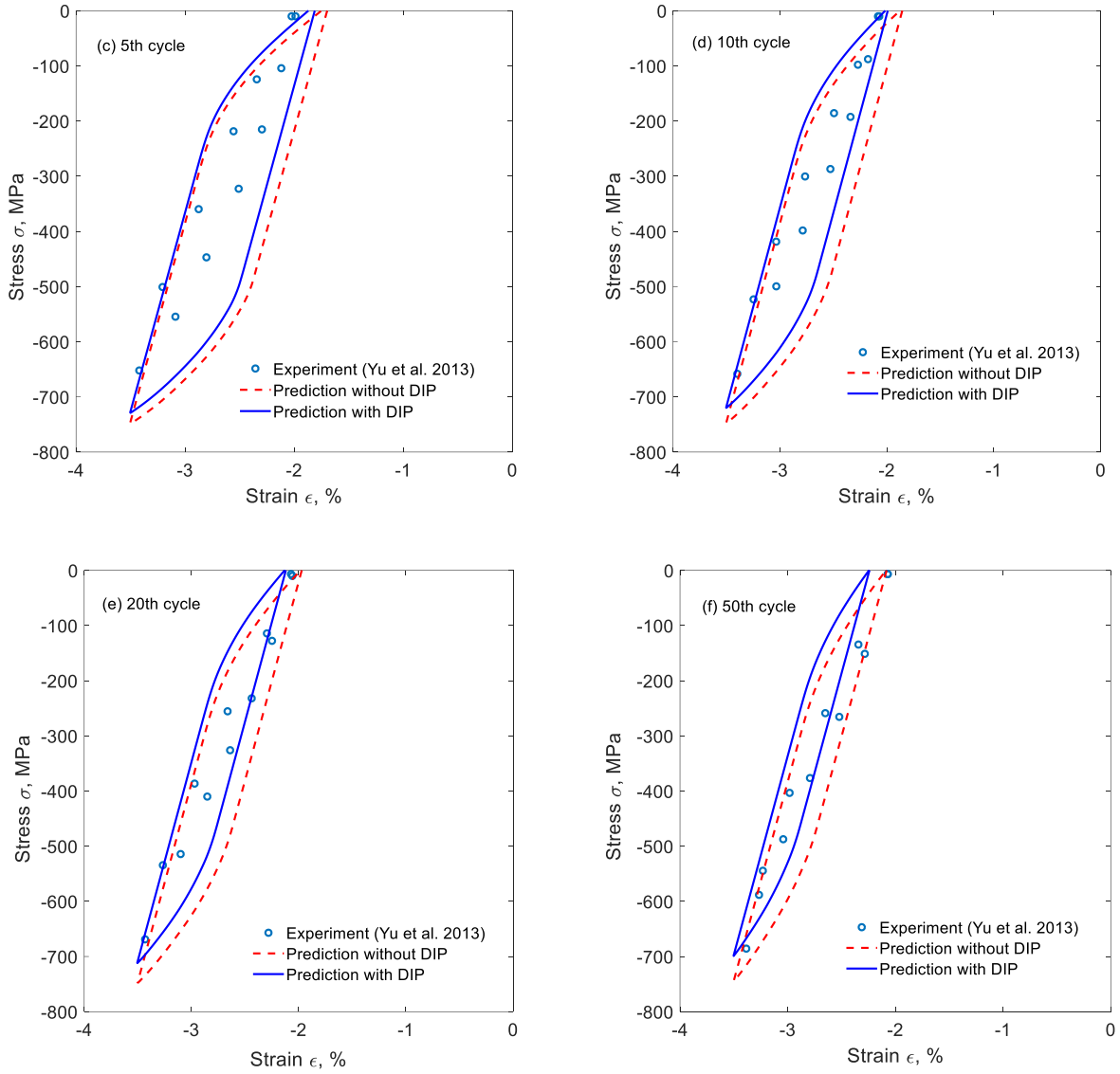

Fig. 10. Experimental and predicted stress-strain curves for strain-controlled cyclic compression-unloading tests where the applied strain cycles between a minimum value of -3.5% and a maximum value of 0%: (a) 1st cycle, (b) 2nd cycle, (c) 5th cycle, (d) 10th cycle, (e) 20th cycle, (f) 50th cycle.

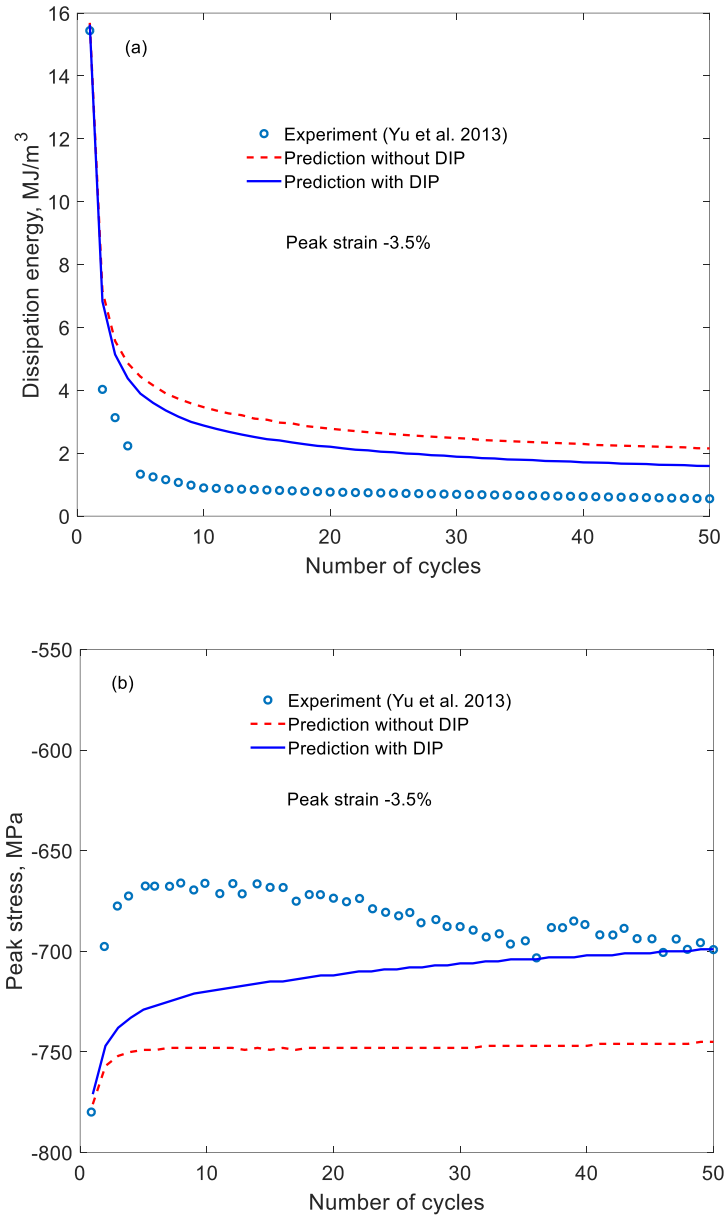

Fig. 11. Experimental and predicted curves for strain-controlled cyclic compression-unloading tests where the applied strain cycles between a minimum value of -3.5% and a maximum value of 0%: (a) dissipation energy vs. number of cycles, (b) peak stress vs. number of cycles.

Fig. 12 shows predicted and experimentally measured stress-strain curves for cyclic tension-unloading with a maximum applied strain of 3.5% and a minimum applied strain of 0%. DIP is not predicted to contribute to the material response, due to the absence of compressive stress through the loading history. Predicted stress-strain curves and predicted evolution of dissipated energy, residual strain and peak tensile stress are shown to follow a similar trend to the experimental measurements of Yu et al. (2013).

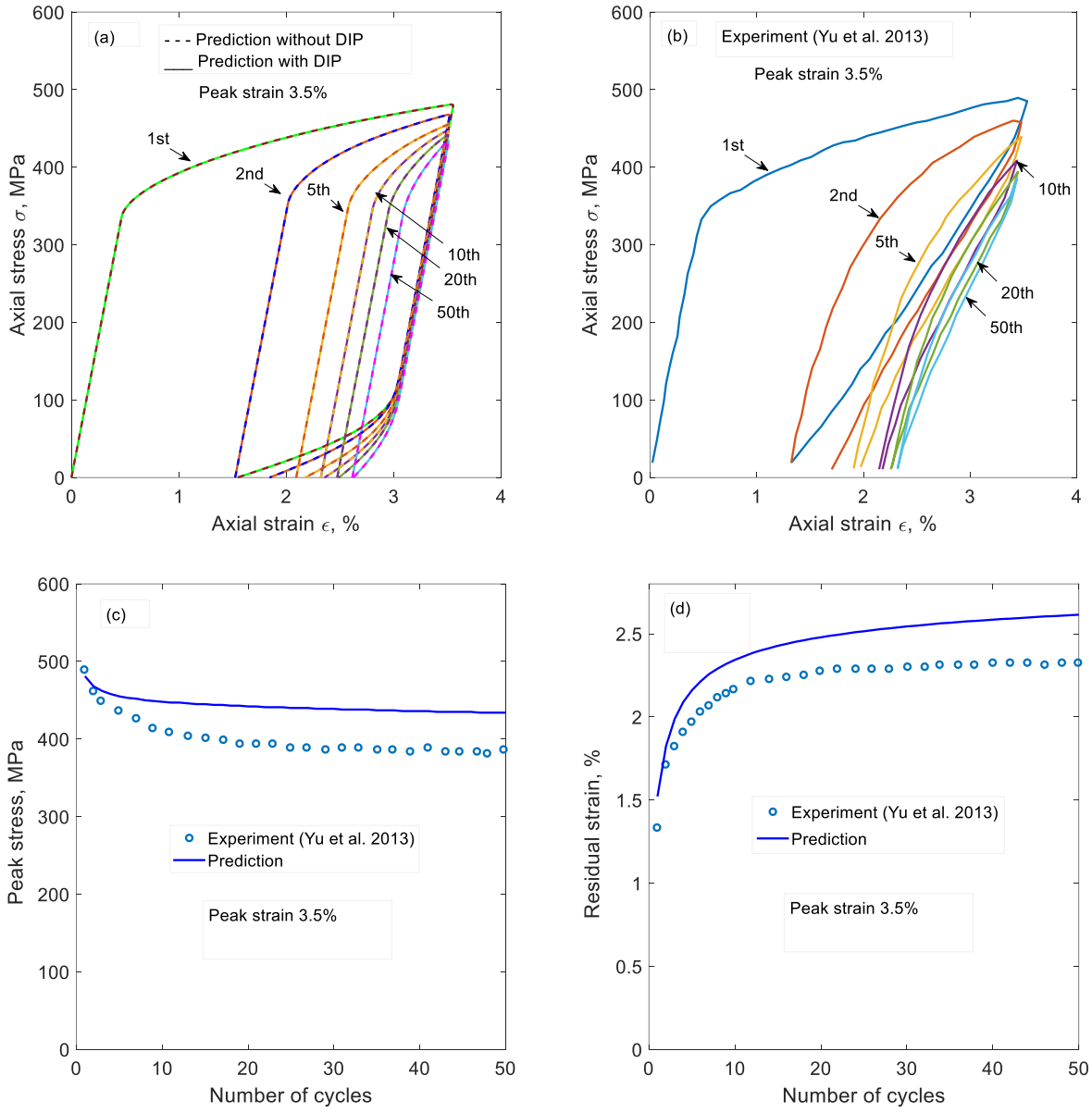
(a)
- - - Prediction without DIP
___ Prediction with DIP
Peak strain 3.5%
1st
2nd
5th
10th
20th
50th
Axial stress σ, MPa
Axial strain ϵ, %
(b)
Experiment (Yu et al. 2013)
Peak strain 3.5%
1st
2nd
5th
10th
20th
50th
Axial stress σ, MPa
Axial strain ϵ, %
(c)
Experiment (Yu et al. 2013)
Prediction
Peak strain 3.5%
Peak stress, MPa
Number of cycles
(d)
Experiment (Yu et al. 2013)
Prediction
Peak strain 3.5%
Residual strain, %
Number of cycles

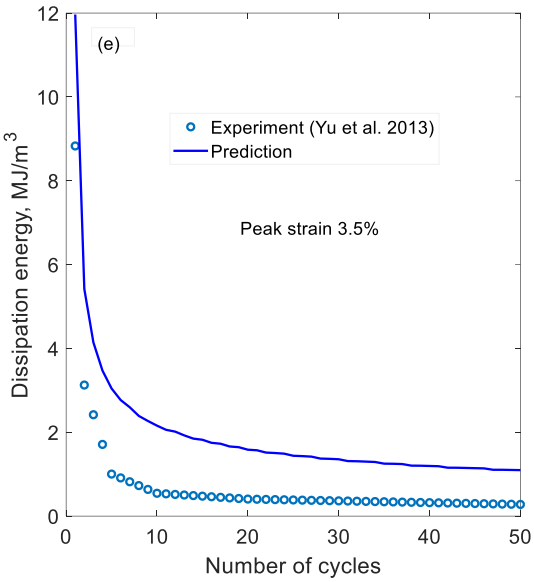

Fig. 12. Experimental and predicted stress-strain curves for strain-controlled cyclic tension-unloading tests where the applied strain cycles between a minimum value of 0% and a maximum value of 3.5%: (a) simulated stress-strain curves, where dashed and solid lines represent simulation without and with considering DIP, respectively, (b) experimental stress-strain curves, (c) peak stress vs. number of cycles, (d) residual strain vs. number of cycles, (e) dissipation energy vs. number of cycles.

Based on the experimental work done by Liu et al. (1998), the effect of DIP is significant under compressive loading while in tension no significant difference is observed with and without considering DIP. The model results presented in this section demonstrate that the inclusion of DIP provides improved predictions of experimentally observed response of NiTi SMAs to cyclic stress- and strain- controlled loading where compressive stress is generated for part, or all, of the loading history.

5. Conclusions

Based on thermodynamic considerations a new inelastic mechanism, detwinning-induced plasticity (DIP), is proposed for modelling the response of NiTi SMAs to cyclic loading. DIP is incorporated into a constitutive framework for NiTi SMA. The constitutive framework also includes well-established inelastic mechanisms of phase transformation, transformation-induced plasticity, residual martensite, and detwinning. The model is constructed at the single crystal scale using the framework of thermodynamics and a crystal plasticity formulation. An explicit scale-

transition rule is used to extend the framework for the analysis of polycrystalline materials, thus facilitating simulation of published experimental test data.

Thermodynamic considerations are used to motivate the contribution of DIP for cyclic loading regimes where compressive stress occurs during part of the loading cycle. However, the contribution of DIP is negligible for cyclic loading regimes that result exclusively in tensile stress. This thermodynamically motivated dependence of DIP on compression, but not on tension, is strongly supported by experimental cyclic loading results of Liu et al. (1998). Inclusion of DIP in a modelling framework results in improved prediction of experimentally observed NiTi SMAs behavior, including strain-controlled cyclic compression-unloading and cyclic tension-unloading tests by Yu et al. (2013) and stress-controlled cyclic tension-compression and tension-unloading tests by Kang et al. (2009). During the first loading cycle the contribution of DIP is not significant in any loading regime. However, in cases where compressive stress occurs during part of the loading cycle, DIP contributes strongly to the material response from the second cycle onwards. In strain-controlled cyclic compression-unloading tests DIP leads to a less negative peak stress and a more negative residual strain following several loading cycles. In stress-controlled tension-compression loading, DIP leads to a reduction of peak and residual strains following loading cycles.

Future applications of the model should consider non-proportional loading and the effects of reorientation and reorientation-induced plasticity (Yu et al., 2015). Ongoing developments of this modelling framework entail the implementation of DIP in a finite element crystal-plasticity modelling framework (McCarthy et al., 2014; McGarry et al., 2007), facilitating the simulation of the mechanical behavior of NiTi SMA stents under long-term cyclic physiological loading regimes.

Appendix

Table A.1: Crystallographic data for the 24 martensite variants in NiTi shape memory alloy (Wang et al., 2008)

α	n_1^α	n_2^α	n_3^α	m_1^α	m_2^α	m_3^α
1	-0.8889	-0.4044	0.2152	0.4114	-0.4981	0.7633
2	-0.4044	-0.8889	-0.2152	-0.4981	0.4114	-0.7633
3	0.8889	0.4044	0.2152	-0.4114	0.4981	0.7633
4	0.4044	0.8889	-0.2152	0.4981	-0.4114	-0.7633
5	-0.8889	0.4044	-0.2152	0.4114	0.4981	-0.7633
6	0.4044	-0.8889	0.2152	0.4981	0.4114	0.7633
7	0.8889	-0.4044	-0.2152	-0.4114	-0.4981	-0.7633
8	-0.4044	0.8889	0.2152	-0.4981	-0.4114	0.7633
9	0.2152	0.8889	0.4044	0.7633	-0.4114	0.4981
10	0.2152	-0.8889	-0.4044	0.7633	0.4114	-0.4981
11	-0.2152	-0.4044	-0.8889	-0.7633	-0.4981	0.4114
12	-0.2152	0.4044	0.8889	-0.7633	0.4981	-0.4114
13	-0.2152	0.8889	-0.4044	-0.7633	-0.4114	-0.4981
14	-0.2152	-0.8889	0.4044	-0.7633	0.4114	0.4981
15	0.2152	0.4044	-0.8889	0.7633	0.4981	0.4114
16	0.2152	-0.4044	0.8889	0.7633	-0.4981	-0.4114
17	0.8889	-0.2152	0.4044	-0.4114	-0.7633	0.4981
18	-0.8889	-0.2152	-0.4044	0.4114	-0.7633	-0.4981
19	0.4044	0.2152	0.8889	0.4981	0.7633	-0.4114
20	-0.4044	0.2152	-0.8889	-0.4981	0.7633	0.4114
21	0.8889	0.2152	-0.4044	-0.4114	0.7633	-0.4981
22	-0.8889	0.2152	0.4044	0.4114	0.7633	0.4981
23	-0.4044	-0.2152	0.8889	-0.4981	-0.7633	-0.4114
24	0.4044	-0.2152	-0.8889	0.4981	-0.7633	0.4114

Table A.2: Crystallographic data for martensite detwinning systems in NiTi shape memory alloy (Thamburaja et al., 2005)

α	a_1^α	a_2^α	a_3^α	w_1^α	w_2^α	w_3^α	λ_0^α
1	-0.5846	0	0.8133	0	0.2804	0	0.271
2	0	-0.5846	-0.8133	0.2804	0	0	0.271
3	-0.5846	0	-0.8133	0	0.2804	0	0.271
4	0	-0.5846	0.8133	0.2804	0	0	0.271
5	-0.5846	0	-0.8133	0	0.2804	0	0.729
6	0	-0.5846	0.8133	0.2804	0	0	0.729
7	-0.5846	0	0.8133	0	0.2804	0	0.729
8	0	-0.5846	-0.8133	0.2804	0	0	0.729
9	-0.8133	-0.5846	0	0	0	0.2804	0.271
10	-0.8133	0.5846	0	0	0	0.2804	0.729
11	-0.8133	0	-0.5846	0	0.2804	0	0.271
12	-0.8133	0	0.5846	0	0.2804	0	0.729
13	-0.8133	0.5846	0	0	0	0.2804	0.271
14	-0.8133	-0.5846	0	0	0	0.2804	0.729
15	-0.8133	0	0.5846	0	0.2804	0	0.271
16	-0.8133	0	-0.5846	0	0.2804	0	0.729
17	0.5846	-0.8133	0	0	0	0.2804	0.729
18	-0.5846	-0.8133	0	0	0	0.2804	0.271
19	0	-0.8133	-0.5846	0.2804	0	0	0.271
20	0	-0.8133	0.5846	0.2804	0	0	0.729
21	-0.5846	-0.8133	0	0	0	0.2804	0.729
22	0.5846	-0.8133	0	0	0	0.2804	0.271
23	0	-0.8133	0.5846	0.2804	0	0	0.271
24	0	-0.8133	-0.5846	0.2804	0	0	0.729

References

Ammar, O., Haddar, N., Dieng, L., 2017. Experimental investigation of the pseudoelastic behaviour of NiTi wires under strain-and stress-controlled cyclic tensile loadings. Intermetallics 81, 52-61.

Anand, L., Gurtin, M.E., 2003. Thermal effects in the superelasticity of crystalline shape-memory materials. Journal of the Mechanics and Physics of Solids 51, 1015-1058.

Arghavani, J., Auricchio, F., Naghdabadi, R., Reali, A., Sohrabpour, S., 2010. A 3-D phenomenological constitutive model for shape memory alloys under multiaxial loadings. International Journal of Plasticity 26, 976-991.

Auricchio, F., Reali, A., Stefanelli, U., 2007. A three-dimensional model describing stress-induced solid phase transformation with permanent inelasticity. International Journal of Plasticity 23, 207-226.

Berveiller, M., Zaoui, A., 1978. An extension of the self-consistent scheme to plastically-flowing polycrystals. Journal of the Mechanics and Physics of Solids 26, 325-344.

Brinson, L.C., Schmidt, I., Lammering, R., 2004. Stress-induced transformation behavior of a polycrystalline NiTi shape memory alloy: Micro and macromechanical investigations via in situ optical microscopy. Journal of the Mechanics and Physics of Solids 52, 1549-1571.

Cailletaud, G., Sai, K., 2008. A polycrystalline model for the description of ratchetting: Effect of intergranular and intragranular hardening. Materials Science and Engineering: A 480, 24-39.

Chen, G., Yin, J., Zhao, S., Tang, H., Qu, X., 2019. Microstructure and tensile properties of a Ti-28Ta alloy studied by transmission electron microscopy and digital image correlation. International Journal of Refractory Metals and Hard Materials 81, 71-77.

Coleman, B.D., Noll, W., 1974. The thermodynamics of elastic materials with heat conduction and viscosity, The Foundations of Mechanics and Thermodynamics. Springer, pp. 145-156.

Delville, R., Malard, B., Pilch, J., Sittner, P., Schryvers, D., 2011. Transmission electron microscopy investigation of dislocation slip during superelastic cycling of Ni–Ti wires. International Journal of Plasticity 27, 282-297.

Dhala, S., Mishra, S., Tewari, A., Alankar, A., 2019. Modeling of finite deformation of pseudoelastic NiTi shape memory alloy considering various inelasticity mechanisms. International Journal of Plasticity 115, 216-237.

Eggeler, G., Hornbogen, E., Yawny, A., Heckmann, A., Wagner, M., 2004. Structural and functional fatigue of NiTi shape memory alloys. Materials Science and Engineering: A 378, 24-33.

Gall, K., Sehitoglu, H., Anderson, R., Karaman, I., Chumlyakov, Y.I., Kireeva, I.V., 2001. On the mechanical behavior of single crystal NiTi shape memory alloys and related polycrystalline phenomenon. Materials Science and Engineering A 317, 85-92.

Hartl, D., Lagoudas, D.C., 2007. Aerospace applications of shape memory alloys. Proceedings of the Institution of Mechanical Engineers, Part G: Journal of Aerospace Engineering 221, 535-552.

Hill, R., 1965. A self-consistent mechanics of composite materials. Journal of the Mechanics and Physics of Solids 13, 213-222.

Kang, G., Bruhns, O.T., Sai, K., 2011. Cyclic polycrystalline visco-plastic model for ratchetting of 316L stainless steel. Computational Materials Science 50, 1399-1405.

Kang, G., Kan, Q., Qian, L., Liu, Y., 2009. Ratchetting deformation of super-elastic and shape-memory NiTi alloys. Mechanics of Materials 41, 139-153.

Kröner, E., 1961. Zurplastischenverformungdesvielkristalls. Acta Metallurgica9.

Lagoudas, D., Hartl, D., Chemisky, Y., Machado, L., Popov, P., 2012. Constitutive model for the numerical analysis of phase transformation in polycrystalline shape memory alloys. International Journal of Plasticity 32, 155-183.

Lagoudas, D.C., 2008. Shape memory alloys: modeling and engineering applications. Springer.

Lagoudas, D.C., Entchev, P.B., 2004. Modeling of transformation-induced plasticity and its effect on the behavior of porous shape memory alloys. Part I: constitutive model for fully dense SMAs. Mechanics of Materials 36, 865-892.

Liu, Y., 2002. On the Detwinning Mechanism in Shape Memory Alloys, IUTAM Symposium on Mechanics of Martensitic Phase Transformation in Solids. Springer, pp. 37-44.

Liu, Y., Xie, Z., 2007. Detwinning in shape memory alloy. Progress in Smart Materials and Structures, Nova Science Publishers Inc, 29-65.

Liu, Y., Xie, Z., Van Humbeeck, J., Delaey, L., 1998. Asymmetry of stress–strain curves under tension and compression for NiTi shape memory alloys. Acta Materialia 46, 4325-4338.

Manchiraju, S., Anderson, P., 2010. Coupling between martensitic phase transformations and plasticity: A microstructure-based finite element model. International Journal of Plasticity 26, 1508-1526.

McCarthy, O., McGarry, J., Leen, S., 2014. The effect of grain orientation on fretting fatigue plasticity and life prediction. Tribology international 76, 100-115.

McGarry, J.P., O'Donnell, B.P., McHugh, P.E., O'Cearbhaill, E., McMeeking, R.M., 2007. Computational examination of the effect of material lnhomogeneity on the necking of stent struts under tensile loading. J. Appl. Mech. Trans. ASME. 74, 978–989. https://doi.org/10.1115/1.2722776

Nemat-Nasser, S., Guo, W.-G., 2006. Superelastic and cyclic response of NiTi SMA at various strain rates and temperatures. Mechanics of materials 38, 463-474.

Otsuka, K., Ren, X., 1999. Recent developments in the research of shape memory alloys. Intermetallics 7, 511-528.

Panico, M., Brinson, L., 2007. A three-dimensional phenomenological model for martensite reorientation in shape memory alloys. Journal of the Mechanics and Physics of Solids 55, 2491-2511.

Patoor, E., Lagoudas, D.C., Entchev, P.B., Brinson, L.C., Gao, X., 2006. Shape memory alloys, Part I: General properties and modeling of single crystals. Mechanics of Materials 38, 391-429.

Saleeb, A., Kumar, A., Padula II, S., Dhakal, B., 2013. The cyclic and evolutionary response to approach the attraction loops under stress controlled isothermal conditions for a multi-mechanism based multi-axial SMA model. Mechanics of Materials 63, 21-47.

Song, D., Kang, G., Kan, Q., Yu, C., Zhang, C., 2014. The effect of martensite plasticity on the cyclic deformation of super-elastic NiTi shape memory alloy. Smart Materials and Structures 23, 015008.

Thamburaja, P., 2005. Constitutive equations for martensitic reorientation and detwinning in shape-memory alloys. Journal of the Mechanics and Physics of Solids 53, 825-856.

Thamburaja, P., Anand, L., 2001. Polycrystalline shape-memory materials: effect of crystallographic texture. Journal of the Mechanics and Physics of Solids 49, 709-737.

Thamburaja, P., Pan, H., Chau, F., 2005. Martensitic reorientation and shape-memory effect in initially textured polycrystalline Ti–Ni sheet. Acta materialia 53, 3821-3831.

Wang, X., Xu, B., Yue, Z., 2008. Micromechanical modelling of the effect of plastic deformation on the mechanical behaviour in pseudoelastic shape memory alloys. International Journal of Plasticity 24, 1307-1332.

Xiao, Y., Zeng, P., Lei, L., 2018. Micromechanical modeling on thermomechanical coupling of cyclically deformed superelastic NiTi shape memory alloy. International Journal of Plasticity 107, 164-188.

Xie, Z., Liu, Y., Van Humbeeck, J., 1998. Microstructure of NiTi shape memory alloy due to tension–compression cyclic deformation. Acta Materialia 46, 1989-2000.

Xu, L., Baxevanis, T., Lagoudas, D.C., 2019. A three-dimensional constitutive model for the martensitic transformation in polycrystalline shape memory alloys under large deformation. Smart Materials and Structures 28, 074004.

Yu, C., Kang, G., Kan, Q., 2014. Crystal plasticity based constitutive model of NiTi shape memory alloy considering different mechanisms of inelastic deformation. International Journal of Plasticity 54, 132-162.

Yu, C., Kang, G., Kan, Q., Song, D., 2013. A micromechanical constitutive model based on crystal plasticity for thermo-mechanical cyclic deformation of NiTi shape memory alloys. International Journal of Plasticity 44, 161-191.

Yu, C., Kang, G., Song, D., Kan, Q., 2012. Micromechanical constitutive model considering plasticity for super-elastic NiTi shape memory alloy. Computational Materials Science 56, 1-5.

Yu, C., Kang, G., Song, D., Kan, Q., 2015. Effect of Martensite Reorientation and Reorientation-induced plasticity on Multiaxial Transformation Ratchetting of Super-elastic NiTi Shape Memory Alloy: New Consideration in Constitutive Model. International Journal of Plasticity.

Zaki, W., Moumni, Z., 2007. A three-dimensional model of the thermomechanical behavior of shape memory alloys. Journal of the Mechanics and Physics of Solids 55, 2455-2490.